MULTIPLE-PARAMETER OPTIMIZATION OF THE SLN SPECT /CT IMAGING PROTOCOL USING MONTE CARLO SIMULATION FOR PRECISION MEDICINE

by

Hilal Yıldız

B.S., Biomedical Engineering, Namık Kemal University, 2014

Submitted to the Institute of Biomedical Engineering
in partial fulfillment of the requirements
for the degree of
Master of Science
in
Biomedical Engineering

Boğaziçi University
2019

ACKNOWLEDGMENTS

I would like to thank sincerely to my thesis advisor Assoc. Prof. Dr. Albert Güveniş who supported me throughout my work and helped me get results of better quality.

I would also like to thank my family and my boyfriend for encouraging me throughout this thesis and my life in general.

ACADEMIC ETHICS AND INTEGRITY STATEMENT

I, Hilal Yıldız, hereby certify that I am aware of the Academic Ethics and Integrity Policy issued by the Council of Higher Education (YÖK) and I fully acknowledge all the consequences due to its violation by plagiarism or any other way.

Name :

Signature:

Date:

ABSTRACT

MULTIPLE-PARAMETER OPTIMIZATION OF THE SLN SPECT /CT IMAGING PROTOCOL USING MONTE CARLO SIMULATION FOR PRECISION MEDICINE

The most encountered cancer type among women is the breast cancer. Advanced clinical treatment applications are currently present, and the effectiveness of treatment is closely related to early diagnosis. Detectability of sentinel lymph nodes (SLNs) in breast assumes noteworthy role in order to predict breast cancer before metastasis. This study intended to scan SLNs in breast by using SPECT/CT and to enhance image quality of SLNs and find out optimal values of different parameters by using the design of experiments methods. The SIMIND Monte Carlo Simulation package and Design of Experiments were used to evaluate SLNs in breast. A Zubal torso phantom was modelled. Typical imaging conditions were utilized from published guidelines and literature. The OSEM algorithms were used for reconstruction. Seven parameters were specified as attenuation correction(+ ; -), number of projections (120; 90), collimator type (low- energy-high-resolution (LEHR); low-energy-general-purpose (LEGP)), energy window (20%; 15%), iteration number (20; 10), subset (15 ; 5) and count activity. An orthogonal array with 8 experimental runs was used. Contrast-to-noise ratios were calculated from lesion and background statistics. From the response table, the highest CNR value was found 9.63 with a combination of LEHR collimator type, attenuation correction, 20% energy window, 20 iterations, 15 subsets, 120 projections and higher count activity. According to results, collimator type, number of projections and attenuation correction had the highest effect. More research is needed to include other correction algorithms.

Keywords: sentinel lymph nodes, SPECT/CT, Monte Carlo simulation, breast.

ÖZET

SPECT/CT GÖRÜNTÜLEME PROTOKOLÜNÜ KULLANARAK MONTE CARLO SİMÜLASYONU ile SLN'in ÇOKLU PARAMETRE OPTİMİZASYONU

Kadınlar arasında en çok görülen kanser türü meme kanseridir. Günümüzde ileri tedavi uygulamaları mevcuttur ve tedavinin etkisi erken teşhisle ilişkilidir. Memedeki sentinel lenf nodüllerinin belirlenebilirliği yayılma olmadan önce meme kanserini tahmin etmek hususunda önemli bir rol üstlenir. Bu çalışma SPECT/CT kullanarak memedeki sentinel lenf nodüllerinin taranması ve sentinel lenf nodüllerinin görüntü kalitesinin gelişmesini ve farklı parametrelerin optimum değerlerinin DOE metodu kullanarak bulunmasını amaçlamıştır. Memedeki sentinel lenf nodüllerinin değerlendirilmesi için SIMIND Monte Carlo Simülasyon paketi ve DOE metodu kullanıldı. Kollar ve bacaklar olmaksızın Zubal gvde modellendi. Yayınlanmış kılavuzlar ve literatürdeki tipik görüntü şartları kullanıldı. OSEM algoritmaları rekonstrüksiyon için kullanıldı. Yedi parametre belirlendi. Bunlar zayıflama düzeltmesi (+; -), projeksiyon sayısı (120; 60), enerji penceresi (%20; %15), kolimatör türü (düşük enerji yüksek rezolüsyonlu (LEHR); düşük enerji genel amaçlı (LEGP)), yineleme sayısı (20; 10), altküme sayısı (15; 5) ve aktivitesiydi. 8 deneysel çalışmayla ortogonal bir dizi kullanıldı. Kontrastın gürültüye oranı hesaplandı. Sonuç tablosuna göre en yüksek kontrat gürültü oranı birinci deneyle 9.63 olarak bulundu. Bu sonuç LEHR kolimatör türü,120 projeksiyon sayısı, zayıflama düzeltmesi yapılarak, %20 enerji penceresi seçilerek, 20 yineleme ve 15 altküme sayısı kullanılarak ve yüksek aktivite kullanılarak elde edildi. İlk sonuçlara göre, kolimatör türü, projeksiyon sayısı ve zayıflama düzeltmesi görüntü kalitesi üzerinde en çok etkiye sahip olan parametreler olarak belirlendi.

Anahtar Sözcükler: sentinel lenf nodülü, SPECT/CT, kanser.

TABLE OF CONTENTS

LIST OF FIGURES

LIST OF TABLES

LIST OF ABBREVIATIONS

AC	Attenuation Correction
SC	Scatter Correction
CoT	Collimator Type
SPECT	Single Photon Emission Computed Tomography
PET	Positron Emission Tomography
CT	Computed Tomography
EW	Energy Window
IT	Iteration Number
SU	Subset
CNR	Contarat to Noise
SLN	Sentinel-Lymph Node
SN	Sentinel Node
OSEM	Ordered Subset Expectation Maximization
LEHR	Low Energy High Resolution
LEGP	Low Energy General Purpose
LMEGP	Low to Medium Energy General Purpose
3D	Three Dimensional
RV	Relative Value
ACo	Activity Concentration
SS	Source Shape
SD	Standard Deviation

1. INTRODUCTION

Nowadays, Cancer is one of the most crucial health issues because of increasing stress, environmental pollution, and unhealthy eating. Various cancer types are available. Yet, their side effects and adverse outcomes are similar and frequently these results can be fatal. Although advanced clinical treatment applications are currently present, these methods are sometimes inadequate. There may be several reasons for this. One of the most critical of these is an inability to detect tumor early and accurately. Sentinel lymph nodes in the breast can be an indicator of breast cancer. Therefore, the detectability of SLN assumes an important role to predict breast cancer before metastasis.

1.1 SPECT Imaging

One of the most common techniques of nuclear medicine imaging is Single Photon Emission Computed Tomography. In SPECT, according to the distribution of the radioactive molecules, three-dimensional images are created due to different directions recording. These 3D images could define the precise properties of the problem [1].

SPECT uses a gamma camera which detects gamma rays emitted by certain radiopharmaceuticals. Each measured signal is sampled in time and space and all SPECT systems use these discrete samples [2]. Step and shoot approach is commonly used in order to measure these signals. In this approach, the camera rotates around the subject and shoots in small predetermined periods.

SPECT is commonly available (with respect to PET) and offers a wide range of studies with a variety of radiopharmaceuticals.

1.2 SPECT Principle

SPECT machine has some characteristics, namely, SPECT uses single photons to create the image, rays are not transmitted like X-ray or not reflected such as ultrasound, Gamma rays are emitted, SPECT machine includes algorithms in its principle, and It offers the opportunity to produce 3D imaging, unlike planar images.

It is a nuclear Medicine imaging modality that contains radionuclides in order to represent the related region and produce 3D functional images by metabolic and physiological information about the organ of interest.

A radiopharmaceutical that injects into the patient's body is emitted further by region of interest. The radiopharmaceutical that usually is preferred as Technetium-99m because of easy to find leads to rays. The rays are called gamma rays and detected by the gamma camera. Gamma rays travel into collimator and this process provides some advantages that are to decrease scatter and enhance image quality. Then the collimated gamma rays hit the crystal detector that converts the gamma rays to visible light. Photo Multiplier Tubes absorb the light and emit the signal. The signals are received from each position, x position, y position, and z position [3]. Design and instrumentation of SPECT are shown in Figure 1.1

1.3 SPECT Image Reconstruction

While gamma camera heads are rotating around the patient, images are usually taken in 2 modes, namely, continuous acquisition, and step and shoot. In general step and shoot method is used. Camera heads stop at specified angles to obtain images in the method. Rotation can be chosen as full 360 or 180 with projection algorithms used to construct for the other half. After acquiring 2D projection images, reconstruction algorithms are used in the axial position [3].

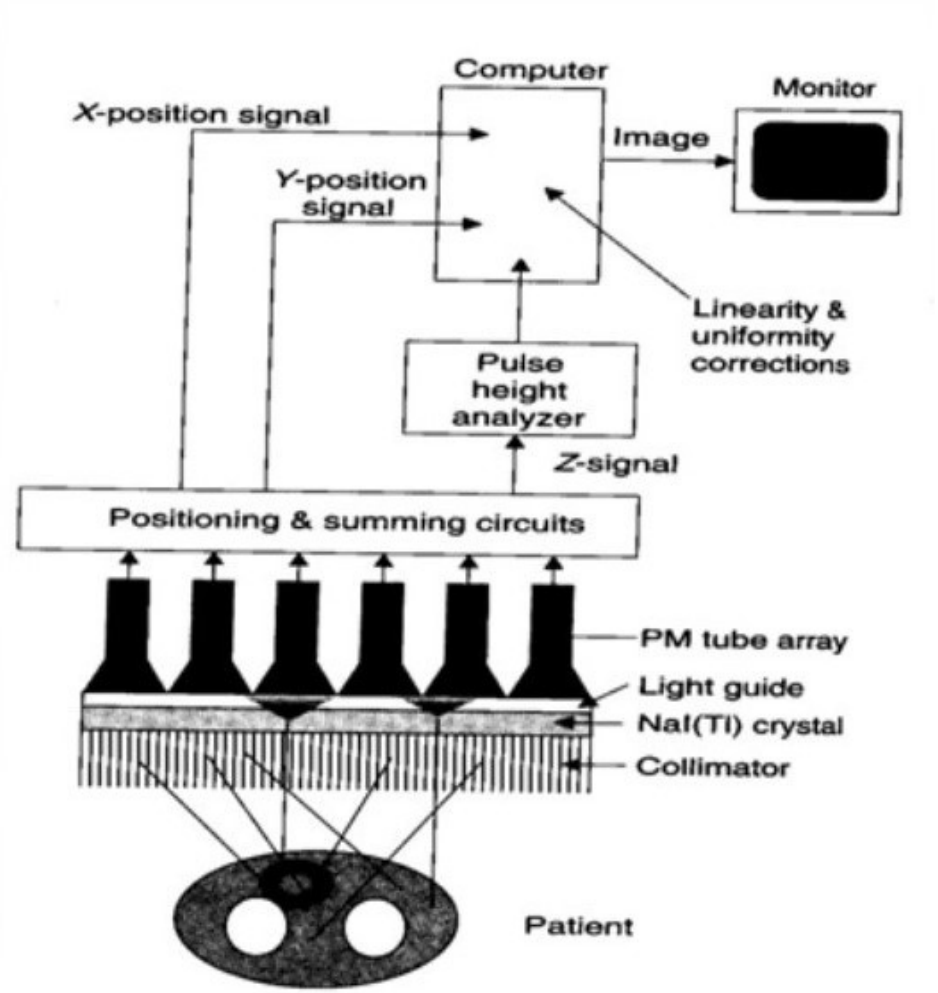

Figure 1.1 Design and Instrumentation.

1.4 Importance of SPECT/CT in Sentinel Lymph Nodes

Single Photon Emission Computed Tomography combined with Computed Tomography (SPECT/CT) is used for various sentinel lymph nodes applications nowadays [4]. This machine has some superiorities such as providing more precise information about the anatomical location of SLNs and obtaining metabolic information in the region of interest.

SPECT/CT brings advantages in the detection of sentinel lymph nodes in breast cancer over planar imaging using the preferred lymphoscintigraphic technique [5]. SPECT/ CT is able both to identify sentinel lymph nodes in a typical localization and to detect sentinel lymph nodes non-visualized on previous planar scans [5]. Precise anatomic localization of sentinel lymph nodes is offered by SPECT/CT, thereby facilitating surgery [6],[7].

Using of SPECT/CT instrumentation parameters has superiorities that both SPECT/CT provides information related to accuracy anatomical location and boosts visualization of SLNs ,[5],[8] especially when SLNs are both unpredictable and close to injection site [9]. However, despite the increasing use of SPECT/CT, it is not entirely exploited for more particular purposes [5]. It means that a similar procedure is applied for each patient. Yet, every patient has a distinct breast structure, different tumor size, and separate tumor location. Therefore, the image quality of each one is not identical.

1.5 State of the Art

Plenty of clinical studies demonstrate that more than 90 percent of SLN cases indicate breast cancer [9]. Increasing the detectability rate of SLN associates with advanced image quality. Therefore, it requires optimization of distinct parameters. Many studies are encountered in the literature related to the optimization of different parameters that affect the image quality of SLNs.

In previous work, Yoneyama et al. have investigated impacts of not only attenuation correction but also scatter correction on image quality of SLNs in the breast that has been obtained by using SPECT/CT [10]. They have matched each possibility of scatter correction and attenuation correction. As a result of that study, findings demonstrate that AC has had an influence upon detection of SLNs positively although SC has created evanescence of slight SLNs in some cases [10].

Another study was carried out by Yoneyama and collogues to boost detection of SLNs by using different collimator types [11]. That study indicated that using the LMEGP that has a lower degree of septal penetration enhanced the visibility of SLN compared with LEHR [11].

1.6 Main Problem

Various parameters have an influence on the visibility of SLNs. A lot of studies are present in literature to optimize different parameters that affect the image quality of SLNs but they include the limited number of parameter and SLN imaging has been optimized by using physical phantom only [3],[11],[12]. In addition to this, the question which parameters have the most influences on the detection ratio of SLNs in the breast has not been answered clearly.

1.7 Objectives

This study aims to optimize the high number of parameters, namely, collimator type, energy window, attenuation correction, projection number, iteration number, subset, and count activity. So, this study is more comprehensive work and offers an opportunity to find out the optimal combination of parameters by design of the experiment. Two main questions of the study are that both which parameters affect image quality mostly and what are the optimal values of these parameters.

1.8 Plan on Thesis

Following parts contain respectively ‘Methods and Materials’, ‘Results’, ‘Discussion’, ‘Conclusions’ and ‘References’ sections.

2. MATERIALS AND METHODS

2.1 Monte Carlo Simulation

SIMIND Monte Carlo Simulation was used by the standard values of SPECT/CT parameters that were acquired from product data of General Electric Infinia Hawkeye Gamma Camera and all data were obtained digitally. Using Monte Carlo Simulation provided a few advantages that were to change instrumentation parameters easily and not much costly [13]. SIMIND system has included two primary programs, change, and simind [14]. Settings of scintillation camera parameters, phantom, SPECT parameters, collimator parameters and image parameters were adjusted by change program. Main page of change program was shown in Figure 2.1. Running of the settings was achieved by simind program [14].

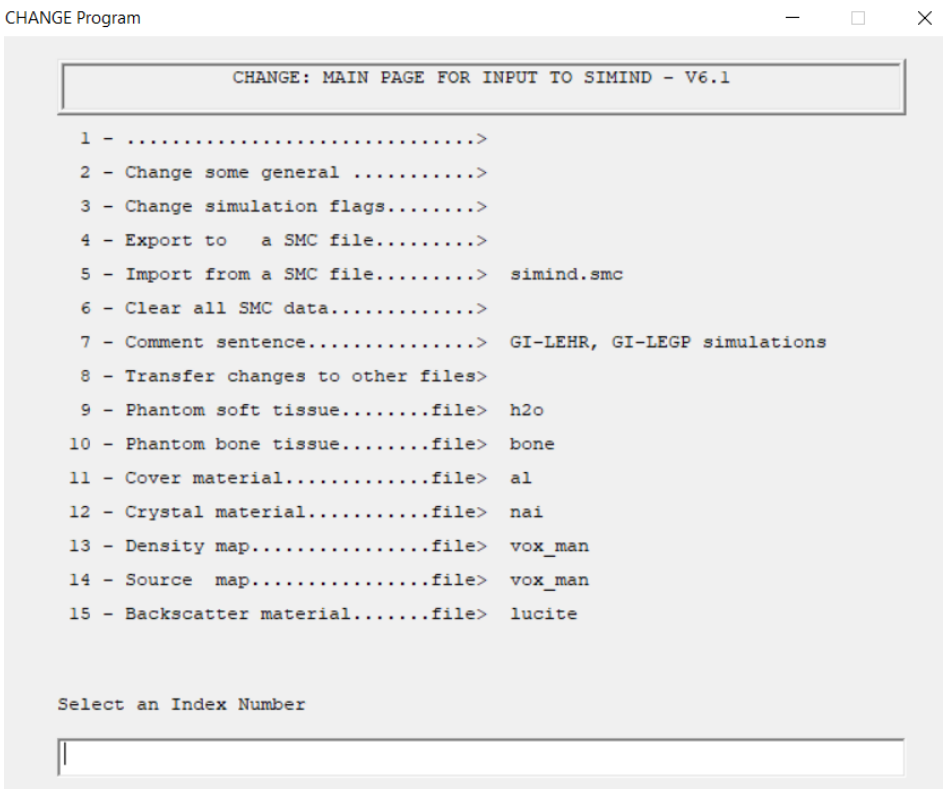

Figure 2.1 Main page of change program.

Crystal settings for General Electric were taken from product data [15] in Table 2.1.

Table 2.1
Crystal Settings.

Crystal Half-Length/radius	27 cm
Crystal Thickness	0.95 cm
Crystal Half-Width	20 cm
Intrinsic Spatial Resolution	3.8 mm
Intrinsic Energy Resolution	9.8 %
Backscattering material thickness	5 cm

Photon energy value, half-length for source and phantom, SPECT rotation, Matrix size Image I and J, Matrix size density map I, Matrix size source map I, Energy Spectra channels and cut-off energy to terminate photon history value were obtained from product data of General Electric Infinia Hawkeye Gamma Camera and articles in literature [15]. Specific codes of phantom type, source type and number of CT-images were applied according to SIMIND manual. The number of CT images for Zubal phantom had to be 243 and phantom and source type had to be -2. Source activity referred to count activity and calculated accordingly voxel sizes of selected organs and ratio of dose to background volume since zubal phantom was used as background for this study [14]. They were demonstrated in Table 2.2.

Two different collimator types, namely low-energy-general purpose, low-energy-high-resolution of General Electric Infinia Hawkeye Gamma Camera were used [15]. Their important parameters' values were taken in SIMIND file [14]. These collimators parameters were demonstrated in Figure 2.2 and in Figure 2.3.

Table 2.2
General Settings.

Photon Energy	140 keV
Source: half-length	30 cm
Phantom: half-length	30 cm
Phantom Type	-2
Source Type	-2
Source Activity	3000 MBq or 6000 MBq
SPECT: No of Projections	90 or 120
SPECT: Rotation	360
Number of CT-images	243
Matrix Size Image I	128
Matrix Size Image J	128
Matrix Size Density Map I	128
Matrix Size Source Map I	128
Energy Spectra Channels	512
Cut-off energy to terminate photon history	92

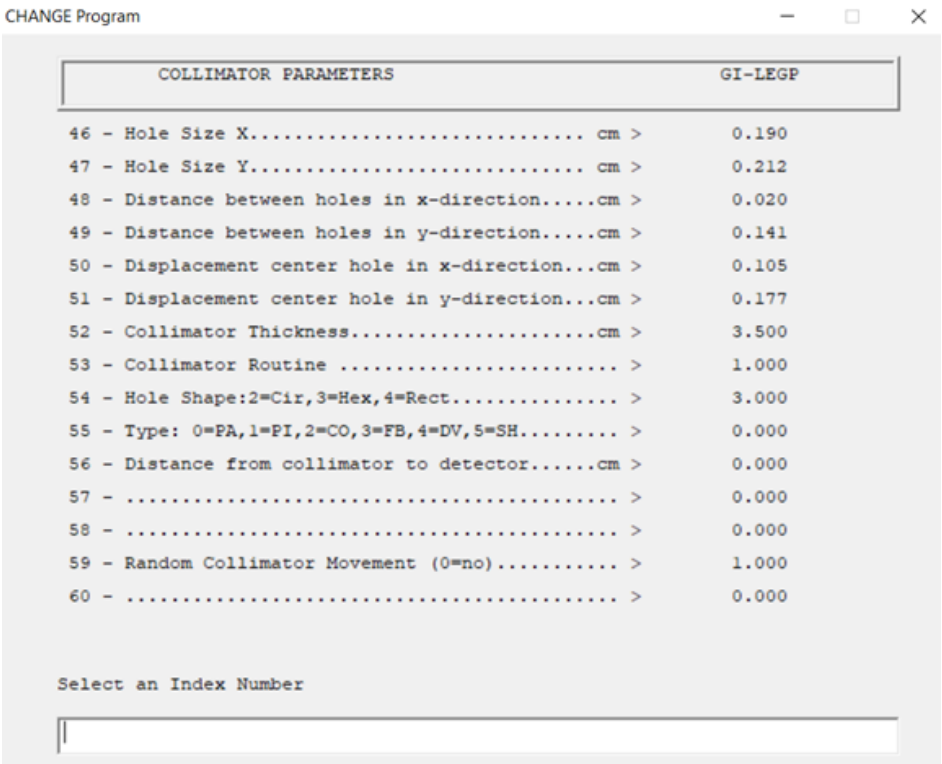

Figure 2.2 Low-energy-general-purpose collimator settings.

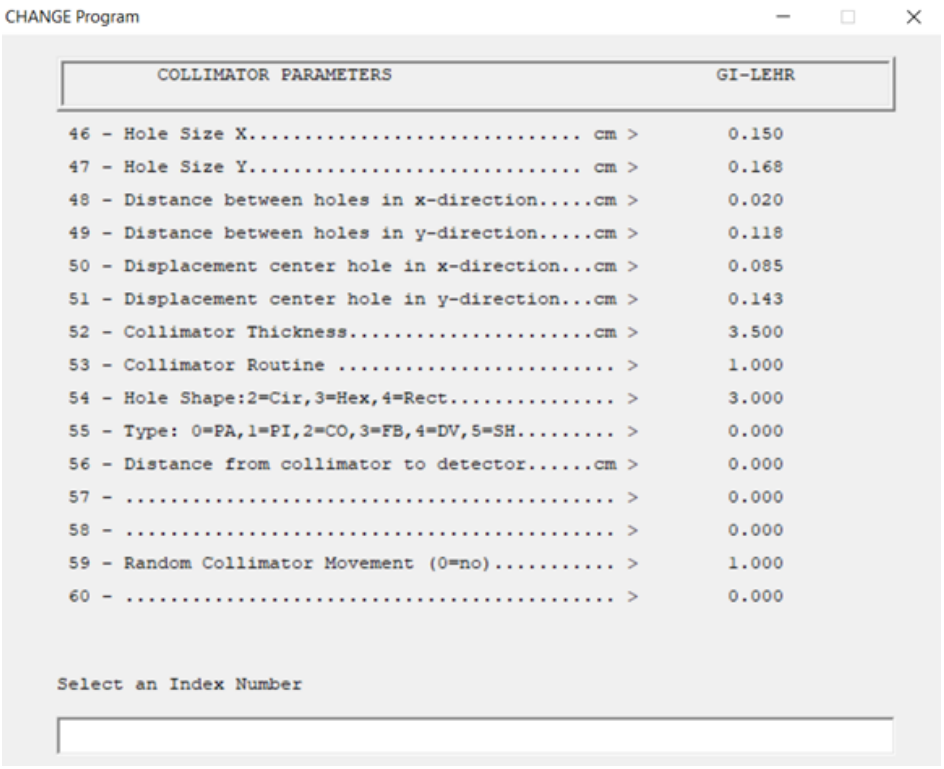

Figure 2.3 Low-energy-high-resolution collimator settings.

2.2 Zubal Phantom

Zubal phantom was used to model the body without legs and arms. Zubal phantom includes more than 50 organs and organ fluids. Organs in torso, lungs, heart, liver, stomach, small bowel, spleen, diaphragm, rib cage sternum and skin were chosen from the zubal file that comprises organ name, the unique code of organ, density value of its organ and relative activity value of its organ for the study [14]. Table 2.3. Zubal phantom can be used for both density mapping and activity mapping. Yet, it was critical and adequate for the study to carry out activity mapping. Controlling to the distribution of density values of organ fluids was a complicated issue because the density of organ fluids such as fat, blood pool was not given separately for each organ. Tumor and injection site were located around the armpit. Their directions for each dimension, size and relative activity values are specified in the input file. Table 2.4.

When the values were appointed, ratios in articles were considered. The ratio of background to Sentinel-lymph-node was taken as 1:20 [16]. In previous works, this ratio is taken between 1:10 and 1:20 [16]. In order to observe changes clearly in the visibility of SLN in the breast, the most ratio in literature was chosen. SLN to injection site ratio was used as 1:20.

2.3 Level Expression of Parameters

Seven distinct parameters, namely attenuation correction, the number of projection, energy window, collimator type, iteration number, subset, and count activity were specified and two different levels were appointed. Table 2.5.

Attenuation correction, values of the number of projection, values of energy window, collimator types, values of iteration numbers, values of subsets were acquired from published articles. According to the guideline for SLN imaging, activities can be used between 3.7 MBq and 370 MBq but up to 150 MBq is usually adequate for

Table 2.3
Zubal Organs.

Organ	Unique Code	Density	Voxel	Relative Activity
skin	1	1090	293757	1
rib cage and sternum	6	1410	31674	1
lungs	10	260	62374	1
heart	11	1060	9354	1
liver	12	1060	30192	1
stomach	17	1030	5133	1
small bowel	18	1030	26447	1
spleen	31	1060	5568	1
diaphragm	39	1030	4528	1

Table 2.4
Tumor and Injection Site Location and Relative Activity Concentration.

	x radius	y radius	z radius	x axis	y axis	z axis	RV of ACo	SS
SLN	1 cm	1 cm	1 cm	84	21	50	20	0
IS	2 cm	2 cm	1 cm	90	27	43	400	0

Table 2.5
Variables and expression levels of parameters of image quality for SLNs in breast.

	AC	Projection No.	EW	CoT	IT	SU	Count Activity
Level 1	+	120	20	LEHR	20	15	6000 MBq
Level 2	-	90	15	LEGP	10	5	3000 MBq

presenting SLNs. However, SLN in this study was chosen 8 voxel size and 1 voxel equals the 4mm, so the size of the SLN has too small size. Tumor size was taken into consideration when determining levels of count activity. Typical value in the guideline(150MBq with 20 seconds) is used for level 1 of count activity and 300 MBq with 20 seconds(6000 MBq) is used for level 2 of count activity.

2.4 Poisson Noise

Poisson noise stems from both the discrete nature of the electric charge and in photon counting in optical devices, where shot noise is associated with the particle nature of light [14]. In other words, Poisson noise occurs naturally, when SPECT/CT runs.

Monte Carlo Simulation ignores adding Poisson noise. For this reason, Poisson noise was added by Image J after image acquisition.

2.5 Design of Experiment by Taguchi Method

Design of experiments is defined as one of the most powerful statistical techniques to study the influence of multivariate parameters simultaneously [17]. Designed experiments have many potential uses in improving processes, including; comparing alternatives, identifying the significant parameters affecting output and achieving an optimal process output [18].

8 experiments for seven apart parameters were created by the program of Minitab'18 with Taguchi method. Combinations of different levels of parameters were applied by using Monte Carlo Simulation (Figure 2.4) and (Table 2.6).

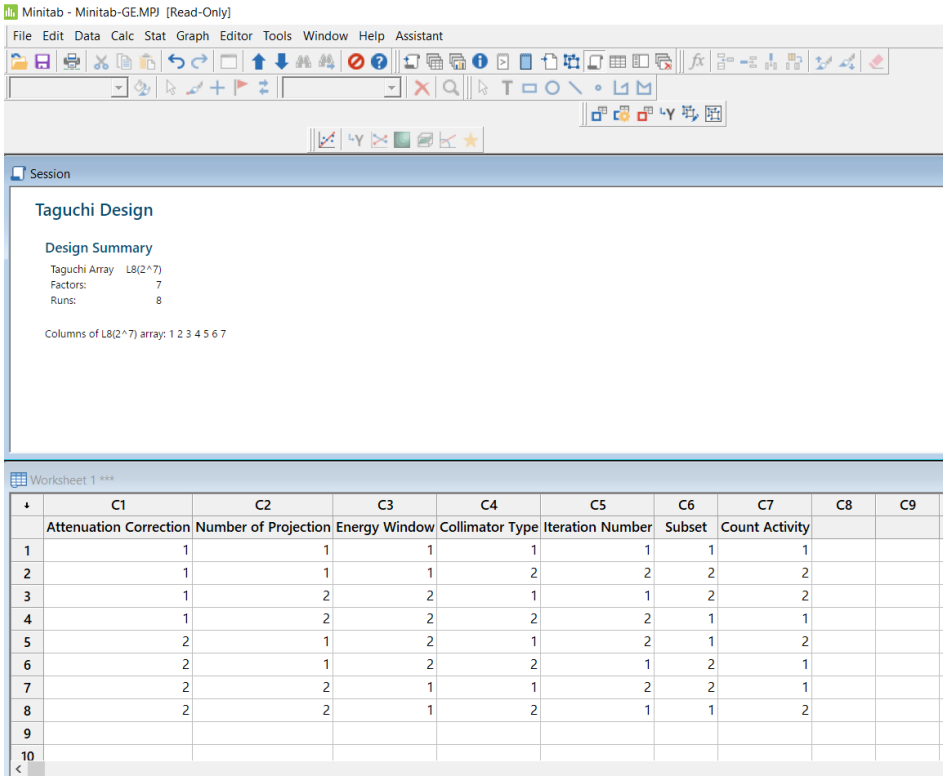

	C1	C2	C3	C4	C5	C6	C7	C8	C9
	Attenuation Correction	Number of Projection	Energy Window	Collimator Type	Iteration Number	Subset	Count Activity		
1	1	1	1	1	1	1	1		
2	1	1	1	2	2	2	2		
3	1	2	2	1	1	2	2		
4	1	2	2	2	2	1	1		
5	2	1	2	1	2	1	2		
6	2	1	2	2	1	2	1		
7	2	2	1	1	2	2	1		
8	2	2	1	2	1	1	2		
9									
10									

Figure 2.4 Taguchi Design.

Table 2.6
Combinations of parameters in experiments.

Experiment. No.	AC	Projection No.	EW	CoT	IT	SU	Activity
Exp.1	+	120	20	LEHR	20	15	6000MBq
Exp.2	+	120	20	LEGP	10	5	3000MBq
Exp.3	+	90	15	LEHR	20	5	3000MBq
Exp.4	+	90	15	LEGP	10	15	6000MBq
Exp.5	-	120	15	LEHR	10	15	3000MBq
Exp.6	-	120	15	LEGP	20	5	6000MBq
Exp.7	-	90	20	LEHR	10	5	6000MBq
Exp.8	-	90	20	LEGP	20	15	3000MBq

2.6 Evaluation Method

CNR was used to evaluate the impacts of parameters and their levels. 3x3 voxel from the lesion and 6x6 voxel from the background that where the pixels were homogeneously distributed and the organs did not overlap were chosen. Different CNR calculations are present in literature. Following formula (Equation 2.1) was used to calculate CNR of each experiment [19].

$$CNR = \frac{(Signal - Background)}{SD(Background)}. \tag{2.1}$$

Signal represents the mean of the lesion, the background represents the mean of background and SD(background) represents the standard deviation of background.

3. RESULTS

3.1 Output File Examples of the SIMIND Phantom Simulation

SIMIND Monte Carlo Simulation created files with .a00 extension, .h00 extension and .res extension [14].

File with .res extension represented the results of the basic detector parameters calculated from the simulation. It also contains input parameters and statistics of the simulation [14].

File with .a00 extension represented the results of simulated SPECT projections. This binary file consists of projection data in 32-bit float format [14].

File with .h00 extension was used for reconstruction. It was the header file [14].

3.1.1 General Electric Infinia Hawkeye Gamma Camera Phantom Simulation Output File for LEHR Collimator

```
              SIMIND Monte Carlo Simulation Program    V6.1
-------------------------------------------------------------------------------
  InputFile: simind         Collimator:pb_sb          SourceFile:smap
  OutputFile:image1         Cover:     al             SourceMap: vox_man
  Phantom(S):h2o            Crystal:   nai            DensityMap:vox_man
  Phantom(B):bone           BackScatt: lucite         ScoreFile: scattwin
-------------------------------------------------------------------------------
  PhotonEnergy              140.00  gi-lehr  PhotonsPerProj          478773
  SourceType           ZubalVoxman  SPECT    Activity              6000.000
```

PhantomType	ZubalVoxman	BScatt	DetectorLenght	29.550
DetectorWidth	22.000	Random	DetectorHeight	0.950
UpperEneWindowTresh	154.000	Phantom	Distance to det	26.500
LowerEneWindowTresh	126.000	Resolut	ShiftSource (X)	0.000
PixelSize (I)	0.400	Forced	ShiftSource (Y)	0.000
PixelSize (J)	0.400	SaveMAP	ShiftSource (Z)	0.000
HalfLength (S)	30.000		HalfLength (P)	30.000
HalfWidth (S)	0.000		HalfWidth (P)	0.000
HalfHeight (S)	0.000		HalfHeigh (P)	0.000
EnergyResolution	9.900		MaxScatterOrder	10

GENERAL DATA

keV/channel	1.000	Compiler	INTEL Windows
Photons/Bq	0.891	StartingAngle	0.000
CameraOffset (X)	0.000	CoverThickness	0.000
CameraOffset (Y)	0.000	BackscatterThickn	5.000
MatrixSize (I)	128	IntrinsicResolut	0.380
MatrixSize (J)	128	AcceptanceAngle	2.743
Emission type	2.000	Initial Weight	0.11166E+05
"NN" Scaling factor	1.000	Energy Channels	512
Photon Exit phantom	1	CutoffEnergy	92.000

Random number generator: ranMar

SPECT DATA

RotationMode	-360.000	Nr of projection	120
RotationAngle	3.000	Projection start	1
Orbital fraction	1.000	Projection end	120

COLLIMATOR DATA FOR ROUTINE:Ray-Tracing by MC

CollimatorCode	gi-lehr	CollimatorType	Parallel
HoleSize (X)	0.150	Distance (X)	0.020
HoleSize (Y)	0.173	Distance (Y)	0.104
CenterShift (X)	0.085	Collimator effic	0.024

CenterShift (Y)	0.147	CollimThickness	3.500
Hole Shape	Hexagonal	Space Coll2Det	0.000
X-Ray flag	0		
CollDepValue (57)	0.000	CollDepValue(58)	0.000
CollDepValue (59)	1.000	CollDepValue(60)	0.000

NON-HOMOGENEOUS PHANTOM DATA

RotationCentre	65, 65	Bone definition	1.190
CT-Pixel size	0.400	Slice thickness	0.247
StartImage	1	No of CT-Images	243
StepSize	0.200	CTmapOrientation	0
MatrixSize (I)	128	MatrixSize (J)	128
CenterPoint (I)	65.000	CenterPoint (J)	65.000
CenterPoint (K)	122.500	ShiftPhantom (X)	0.000
ShiftPhantom (Y)	0.000	ShiftPhantom (Z)	0.000

PHANTOM DATA FROM FILE: simind.zub SECTION: 1

ORGAN	DENSITY	PIXELS	VOLUME(CC)	MBQ	MBQ/CC	VALUE
skin	0.000	293757	0.116E+05	0.368E+04	0.317E+00	1.0
brain	0.000	0	0	0	0	0.0
spinal cord	0.000	0	0	0	0	0.0
skull	0.000	0	0	0	0	0.0
spine	0.000	0	0	0	0	0.0
rib cage & ster	0.000	31674	0.125E+04	0.397E+03	0.317E+00	1.0
pelvis	0.000	0	0	0	0	0.0
long bones	0.000	0	0	0	0	0.0
skeletal muscle	0.000	0	0	0	0	0.0
lungs	0.000	62374	0.246E+04	0.782E+03	0.317E+00	1.0
heart	0.000	9354	0.370E+03	0.117E+03	0.317E+00	1.0
liver	0.000	30192	0.119E+04	0.378E+03	0.317E+00	1.0
gall bladder	0.000	0	0	0	0	0.0
kidney	0.000	0	0	0	0	0.0
pharynx	0.000	0	0	0	0	0.0

esophagus	0.000	0	0	0	0	0.0
stomach	0.000	5133	0.203E+03	0.643E+02	0.317E+00	1.0
small bowel	0.000	26447	0.104E+04	0.331E+03	0.317E+00	1.0
colon	0.000	0	0	0	0	0.0
pancreas	0.000	0	0	0	0	0.0
adrenals	0.000	0	0	0	0	0.0
fat	0.000	0	0	0	0	0.0
blood pool	0.000	0	0	0	0	0.0
gas (bowel)	0.000	0	0	0	0	0.0
fluid (bowel)	0.000	0	0	0	0	0.0
bone marrow	0.000	0	0	0	0	0.0
lymph nodes	0.000	0	0	0	0	0.0
thyroid	0.000	0	0	0	0	0.0
trachea	0.000	0	0	0	0	0.0
cartilage	0.000	0	0	0	0	0.0
spleen	0.000	5568	0.220E+03	0.698E+02	0.317E+00	1.0
urine	0.000	0	0	0	0	0.0
feces	0.000	0	0	0	0	0.0
testes	0.000	0	0	0	0	0.0
prostate	0.000	0	0	0	0	0.0
rectum	0.000	0	0	0	0	0.0
diaphragm	0.000	4528	0.179E+03	0.567E+02	0.317E+00	1.0
bladder	0.000	0	0	0	0	0.0
lesion	0.000	0	0	0	0	0.0
dens of axis	0.000	0	0	0	0	0.0
jaw bone	0.000	0	0	0	0	0.0
lacrimal glands	0.000	0	0	0	0	0.0
spinal canal	0.000	0	0	0	0	0.0
hard palate	0.000	0	0	0	0	0.0
cerebellum	0.000	0	0	0	0	0.0
tongue	0.000	0	0	0	0	0.0
medulla oblongo	0.000	0	0	0	0	0.0
pons	0.000	0	0	0	0	0.0
uncus(ear bones	0.000	0	0	0	0	0.0

```
  sinuses           0.000         0           0           0           0     0.0
  optic nerve       0.000         0           0           0           0     0.0
  cerebral falx     0.000         0           0           0           0     0.0
  eye               0.000         0           0           0           0     0.0
  lens              0.000         0           0           0           0     0.0
  cerebral aquadu   0.000         0           0           0           0     0.0
  teeth             0.000         0           0           0           0     0.0
  TUMORS ADDED FROM FILE:simind.inp
  TUMOR  VOL(pix)     VOL(cc)     MBq         MBq/cc   CHANGE g/cm3
    1         8      0.316E+00   0.201E+01   0.634E+01   none
    2        24      0.948E+00   0.120E+03   0.127E+03   none
-------------------------------------------------------------------------------
  SCATTWIN RESULTS USING WINDOW FILE: simind.win

  Win  WinAdded  Range(keV)   ScaleFactor
   1        0    126.0 - 154.0    1.00
   2        1     92.0 - 125.9    1.00

  Win    Total    Scatter   Primary  S/P-Ratio S/T Ratio  Cps/MBq
   1   0.535E+08        0   0.535E+08        0         0    0.743E+02
   2   0.132E+07        0   0.132E+07        0         0    0.183E+01

  Win  Geo(Air)  Pen(Air)  Sca(Air)  Geo(Tot)  Pen(Tot)  Sca(Tot)
   1    95.44%     3.21%     1.35%    95.44%     3.21%     1.35%
   2    93.76%     3.11%     3.13%    93.76%     3.11%     3.13%

-------------------------------------------------------------------------------
  Simulation start: 2019:07:14 16:07:57
  Simulation stop : 2019:07:14 16:11:29
  Elapsed time 0h 3min and 32sec
-------------------------------------------------------------------------------
  INTERACTIONS IN THE CRYSTAL
  Detector hits......:         151562
  Detector hits/sec..:           718.
```

```
  Max val in spectra.:     0.3953E+07
  Max val in images..:     0.7897E+03
  Count rate [Total].:     0.5134E+06
  Count rate [Window]:     0.4793E+06
-------------------------------------------------------------------------------
  PHOTONS AFTER 1) COLLIMATOR AND 2) WITHIN E-WIN
  Geometric.....: 95.41%  95.44%
  Penetration...:  3.21%   3.21%
  Scatter Collim:  1.38%   1.35%
  X-ray Collim..:  0.00%   0.00%
-------------------------------------------------------------------------------
  RESULTS FROM ENERGY SPECTRUM
  Compton area in spectrum:  0.3571E+07    3.84% (1SD)
  Photo   area in spectrum:  0.5752E+08    1.67% (1SD)
  Pileup  area in spectrum:  0.5134E+06    2.20% (1SD)
-------------------------------------------------------------------------------
  CALCULATED DETECTOR PARAMETERS
  Efficiency [Peak]....:      0.8653      1.67% (1SD)
  Efficiency [Detector]:      0.9267
  Sensitivity [cps/MBq]:     79.8906
  Sensitivity [cpm/uCi]:    177.3571
  Peak/Compton [Peak]..:     67.9449
  Peak/Compton [Area]..:     16.1058
  Peak/Total...........:      0.9337

  Inifile: simind.ini
  Comment: EMISSION VMAN
-------------------------------------------------------------------------------
  Command: simind image1/in:x22,5x/if:2
```

3.1.2 General Electric Infinia Hawkeye Gamma Camera Phantom Simulation Output File for LEGP Collimator

SIMIND Monte Carlo Simulation Program V6.1

InputFile: simind		Collimator:pb_sb		SourceFile:smap	
OutputFile:image2		Cover: al		SourceMap: vox_man	
Phantom(S):h2o		Crystal: nai		DensityMap:vox_man	
Phantom(B):bone		BackScatt: lucite		ScoreFile: scattwin	
PhotonEnergy	140.00	gi-legp	PhotonsPerProj		478773
SourceType	ZubalVoxman	SPECT	Activity		3000.000
PhantomType	ZubalVoxman	BScatt	DetectorLenght		29.550
DetectorWidth	22.000	Random	DetectorHeight		0.950
UpperEneWindowTresh	154.000	Phantom	Distance to det		26.500
LowerEneWindowTresh	126.000	Resolut	ShiftSource (X)		0.000
PixelSize (I)	0.400	Forced	ShiftSource (Y)		0.000
PixelSize (J)	0.400	SaveMAP	ShiftSource (Z)		0.000
HalfLength (S)	30.000		HalfLength (P)		30.000
HalfWidth (S)	0.000		HalfWidth (P)		0.000
HalfHeight (S)	0.000		HalfHeigh (P)		0.000
EnergyResolution	9.900		MaxScatterOrder		10
GENERAL DATA					
keV/channel	1.000		Compiler		INTEL Windows
Photons/Bq	0.891		StartingAngle		0.000
CameraOffset (X)	0.000		CoverThickness		0.000
CameraOffset (Y)	0.000		BackscatterThickn		5.000
MatrixSize (I)	128		IntrinsicResolut		0.380
MatrixSize (J)	128		AcceptanceAngle		3.473
Emission type	2.000		Initial Weight		0.55830E+04
"NN" Scaling factor	1.000		Energy Channels		512

Photon Exit phantom	1	CutoffEnergy	92.000

Random number generator: ranMar

SPECT DATA

RotationMode	-360.000	Nr of projection	120
RotationAngle	3.000	Projection start	1
Orbital fraction	1.000	Projection end	120

COLLIMATOR DATA FOR ROUTINE:Ray-Tracing by MC

CollimatorCode	gi-legp	CollimatorType	Parallel
HoleSize (X)	0.190	Distance (X)	0.020
HoleSize (Y)	0.219	Distance (Y)	0.127
CenterShift (X)	0.105	Collimator effic	0.030
CenterShift (Y)	0.182	CollimThickness	3.500
Hole Shape	Hexagonal	Space Coll2Det	0.000
X-Ray flag	0		
CollDepValue (57)	0.000	CollDepValue(58)	0.000
CollDepValue (59)	1.000	CollDepValue(60)	0.000

NON-HOMOGENEOUS PHANTOM DATA

RotationCentre	65, 65	Bone definition	1.190
CT-Pixel size	0.400	Slice thickness	0.247
StartImage	1	No of CT-Images	243
StepSize	0.200	CTmapOrientation	0
MatrixSize (I)	128	MatrixSize (J)	128
CenterPoint (I)	65.000	CenterPoint (J)	65.000
CenterPoint (K)	122.500	ShiftPhantom (X)	0.000
ShiftPhantom (Y)	0.000	ShiftPhantom (Z)	0.000

PHANTOM DATA FROM FILE: simind.zub SECTION: 1

ORGAN	DENSITY	PIXELS	VOLUME(CC)	MBQ	MBQ/CC	VALUE
skin	0.000	293757	0.116E+05	0.184E+04	0.159E+00	1.0

brain	0.000	0	0	0	0	0.0
spinal cord	0.000	0	0	0	0	0.0
skull	0.000	0	0	0	0	0.0
spine	0.000	0	0	0	0	0.0
rib cage & ster	0.000	31674	0.125E+04	0.198E+03	0.159E+00	1.0
pelvis	0.000	0	0	0	0	0.0
long bones	0.000	0	0	0	0	0.0
skeletal muscle	0.000	0	0	0	0	0.0
lungs	0.000	62374	0.246E+04	0.391E+03	0.159E+00	1.0
heart	0.000	9354	0.370E+03	0.586E+02	0.159E+00	1.0
liver	0.000	30192	0.119E+04	0.189E+03	0.159E+00	1.0
gall bladder	0.000	0	0	0	0	0.0
kidney	0.000	0	0	0	0	0.0
pharynx	0.000	0	0	0	0	0.0
esophagus	0.000	0	0	0	0	0.0
stomach	0.000	5133	0.203E+03	0.322E+02	0.159E+00	1.0
small bowel	0.000	26447	0.104E+04	0.166E+03	0.159E+00	1.0
colon	0.000	0	0	0	0	0.0
pancreas	0.000	0	0	0	0	0.0
adrenals	0.000	0	0	0	0	0.0
fat	0.000	0	0	0	0	0.0
blood pool	0.000	0	0	0	0	0.0
gas (bowel)	0.000	0	0	0	0	0.0
fluid (bowel)	0.000	0	0	0	0	0.0
bone marrow	0.000	0	0	0	0	0.0
lymph nodes	0.000	0	0	0	0	0.0
thyroid	0.000	0	0	0	0	0.0
trachea	0.000	0	0	0	0	0.0
cartilage	0.000	0	0	0	0	0.0
spleen	0.000	5568	0.220E+03	0.349E+02	0.159E+00	1.0
urine	0.000	0	0	0	0	0.0
feces	0.000	0	0	0	0	0.0
testes	0.000	0	0	0	0	0.0
prostate	0.000	0	0	0	0	0.0

```
rectum              0.000         0           0           0           0     0.0
diaphragm           0.000      4528   0.179E+03   0.284E+02   0.159E+00     1.0
bladder             0.000         0           0           0           0     0.0
lesion              0.000         0           0           0           0     0.0
dens of axis        0.000         0           0           0           0     0.0
jaw bone            0.000         0           0           0           0     0.0
lacrimal glands     0.000         0           0           0           0     0.0
spinal canal        0.000         0           0           0           0     0.0
hard palate         0.000         0           0           0           0     0.0
cerebellum          0.000         0           0           0           0     0.0
tongue              0.000         0           0           0           0     0.0
medulla oblongo     0.000         0           0           0           0     0.0
pons                0.000         0           0           0           0     0.0
uncus(ear bones     0.000         0           0           0           0     0.0
sinuses             0.000         0           0           0           0     0.0
optic nerve         0.000         0           0           0           0     0.0
cerebral falx       0.000         0           0           0           0     0.0
eye                 0.000         0           0           0           0     0.0
lens                0.000         0           0           0           0     0.0
cerebral aquadu     0.000         0           0           0           0     0.0
teeth               0.000         0           0           0           0     0.0
TUMORS ADDED FROM FILE:simind.inp
TUMOR  VOL(pix)     VOL(cc)     MBq         MBq/cc    CHANGE g/cm3
  1         8      0.316E+00   0.100E+01   0.317E+01    none
  2        24      0.948E+00   0.602E+02   0.634E+02    none
--------------------------------------------------------------------------------
SCATTWIN RESULTS USING WINDOW FILE: simind.win

Win  WinAdded  Range(keV)   ScaleFactor
 1        0    126.0 - 154.0    1.00
 2        1     92.0 - 125.9    1.00

Win    Total    Scatter   Primary  S/P-Ratio S/T Ratio  Cps/MBq
 1   0.451E+08        0   0.451E+08     0          0      0.125E+03
```

2	0.112E+07	0	0.112E+07	0	0	0.310E+01

Win	Geo(Air)	Pen(Air)	Sca(Air)	Geo(Tot)	Pen(Tot)	Sca(Tot)
1	95.50%	3.21%	1.29%	95.50%	3.21%	1.29%
2	93.38%	3.11%	3.51%	93.38%	3.11%	3.51%

```
--------------------------------------------------------------------------------
Simulation start: 2019:07:14 16:12:14
Simulation stop : 2019:07:14 16:16:03
Elapsed time 0h 3min and 49sec
--------------------------------------------------------------------------------
INTERACTIONS IN THE CRYSTAL
Detector hits......:          158646
Detector hits/sec..:            701.
Max val in spectra.:     0.3327E+07
Max val in images..:     0.5238E+03
Count rate [Total].:     0.4323E+06
Count rate [Window]:     0.4037E+06
--------------------------------------------------------------------------------
PHOTONS AFTER 1) COLLIMATOR AND 2) WITHIN E-WIN
Geometric.....: 95.46%  95.51%
Penetration...:  3.20%   3.20%
Scatter Collim:  1.33%   1.29%
X-ray Collim..:  0.00%   0.00%
--------------------------------------------------------------------------------
RESULTS FROM ENERGY SPECTRUM
Compton area in spectrum:  0.3006E+07    3.97% (1SD)
Photo   area in spectrum:  0.4844E+08    1.81% (1SD)
Pileup  area in spectrum:  0.4357E+06    1.94% (1SD)
--------------------------------------------------------------------------------
CALCULATED DETECTOR PARAMETERS
Efficiency [Peak]....:      0.8652      1.81% (1SD)
Efficiency [Detector]:      0.9267
Sensitivity [cps/MBq]:    134.5550
```

```
  Sensitivity [cpm/uCi]:    298.7122
  Peak/Compton [Peak]..:     69.1595
  Peak/Compton [Area]..:     16.1141
  Peak/Total...........:      0.9337

  Inifile: simind.ini
  Comment: EMISSION VMAN
--------------------------------------------------------------------------------
  Command: simind image2/in:x22,5x/if:2
```

3.2 Reconstructed Images and Calculations

3.2.1 Result for experiment 1

Experiment 1 included LEHR collimator type, 120 projections, and higher count activity level. Upper energy window and lower energy window were set respectively 154; 126. When the SPECT/CT simulation was run, the noise was not added automatically. Poisson noise was added by Image J program after the acquisition of image (Figure 3.1).

After Poisson noise was added, OSEM reconstruction algorithm was applied with 20 iteration number and 15 subsets. Attenuation correction was included in image 1 (Figure 3.2) and (Figure 3.3).

CNR was used to evaluate the detectability of SLN.

CNR for reconstructed nuclear image 1: **9.63**.

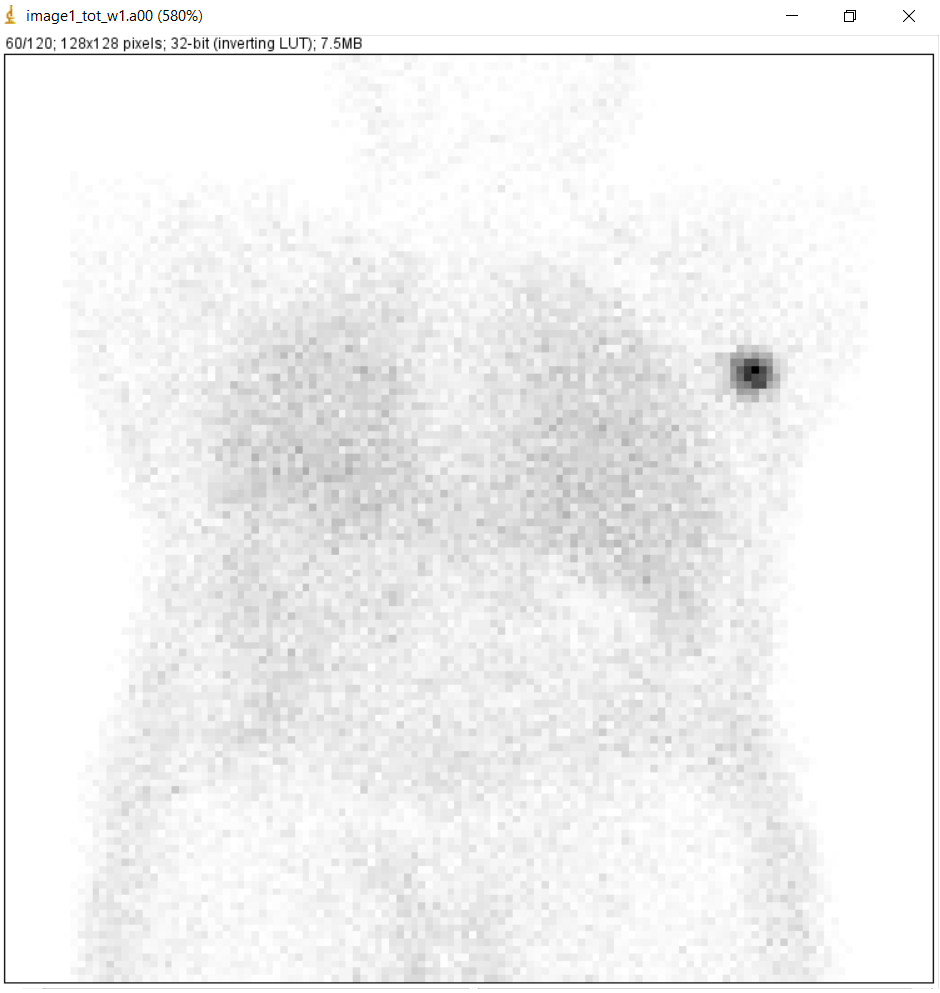

Figure 3.1 View of 60. projection of image 1 with noise.

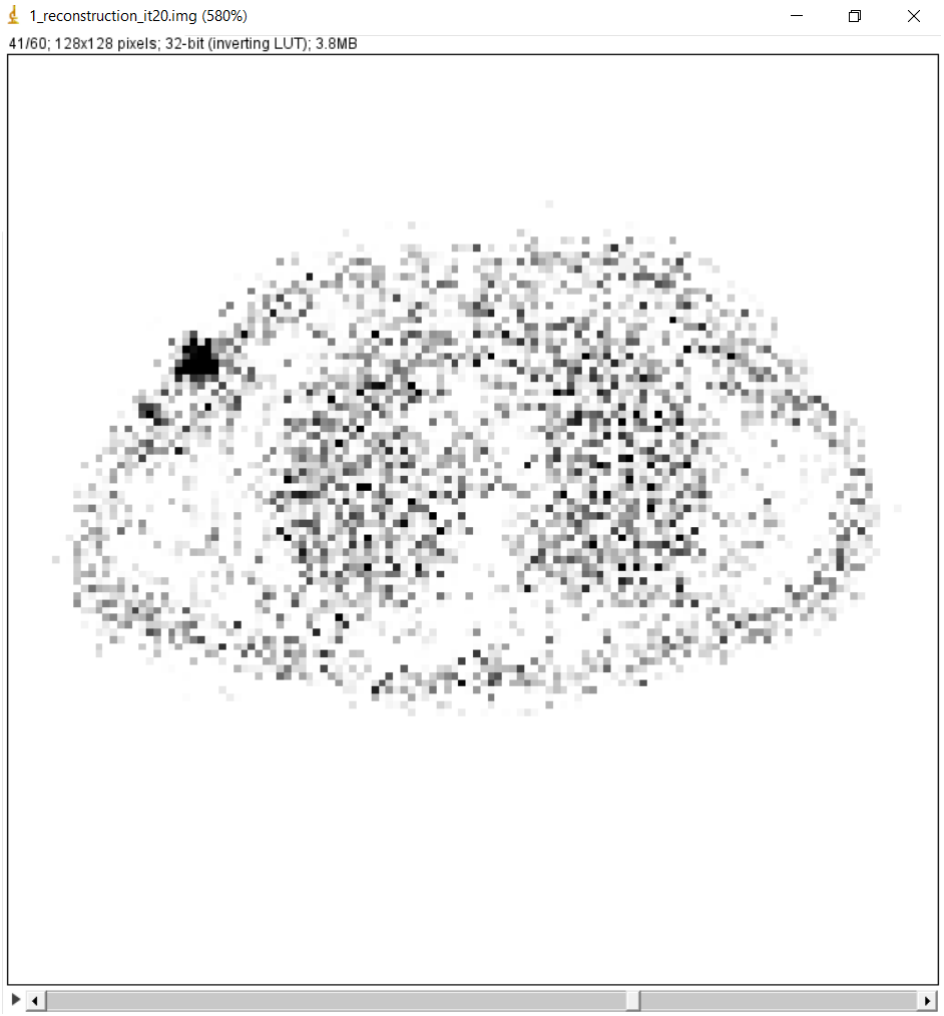

Figure 3.2 View of 41. slice of reconstructed image 1.

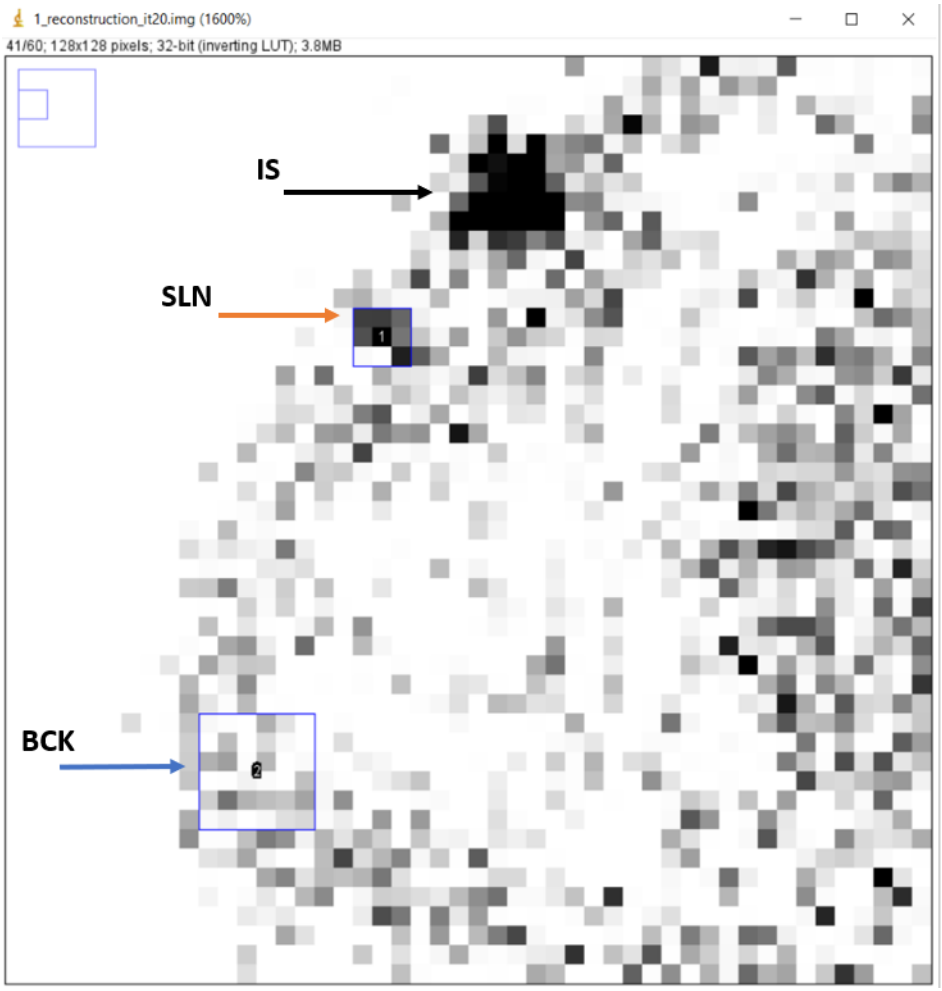

Figure 3.3 Representing to IS, SLN and BCK.

3.2.2 Result for experiment 2

Experiment 2 comprised LEGP collimator type, 120 projections, and lower count activity level. Upper energy window and lower energy window were set respectively 154; 126. When the SPECT/CT simulation was run, the noise was not added automatically. Poisson noise was added by Image J program after the acquisition of image (Figure 3.4).

After Poisson noise was added, OSEM reconstruction algorithm was applied with 10 iteration number and 5 subsets. Attenuation correction was included in image 2 (Figure 3.5) and (Figure 3.6).

CNR was used to evaluate the detectability of SLN.

CNR for reconstructed nuclear image 2: **4.23**.

3.2.3 Result for experiment 3

Experiment 3 comprised LEHR collimator type, 90 projections, and lower count activity level. Upper energy window and lower energy window were set respectively 150.5; 129.5. When the SPECT/CT simulation was run, the noise was not added automatically. Poisson noise was added by Image J program after the acquisition of image (Figure 3.7).

After Poisson noise was added, OSEM reconstruction algorithm was applied with 20 iteration number and 5 subsets. Attenuation correction was included in image 3 (Figure 3.8) and (Figure 3.9).

CNR was used to evaluate the detectability of SLN.

CNR for reconstructed nuclear image 3: **5.4**.

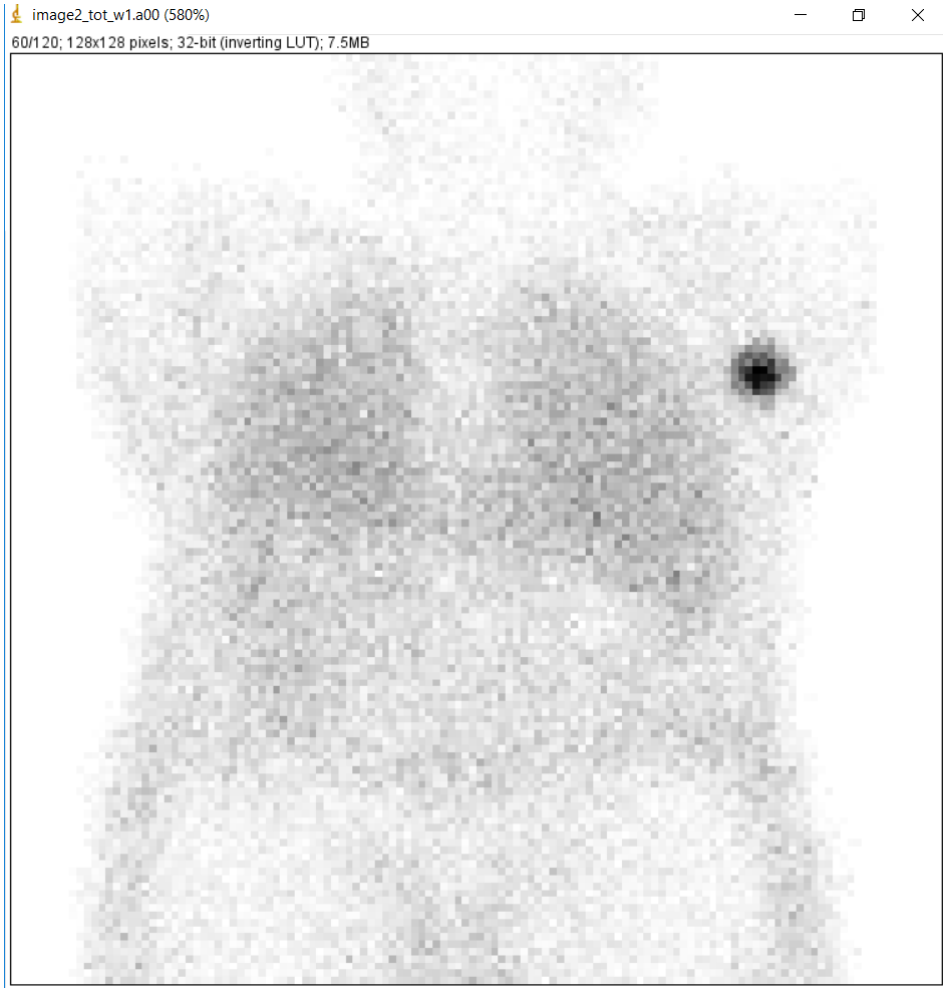

Figure 3.4 View of 60. projection of image 2 with noise.

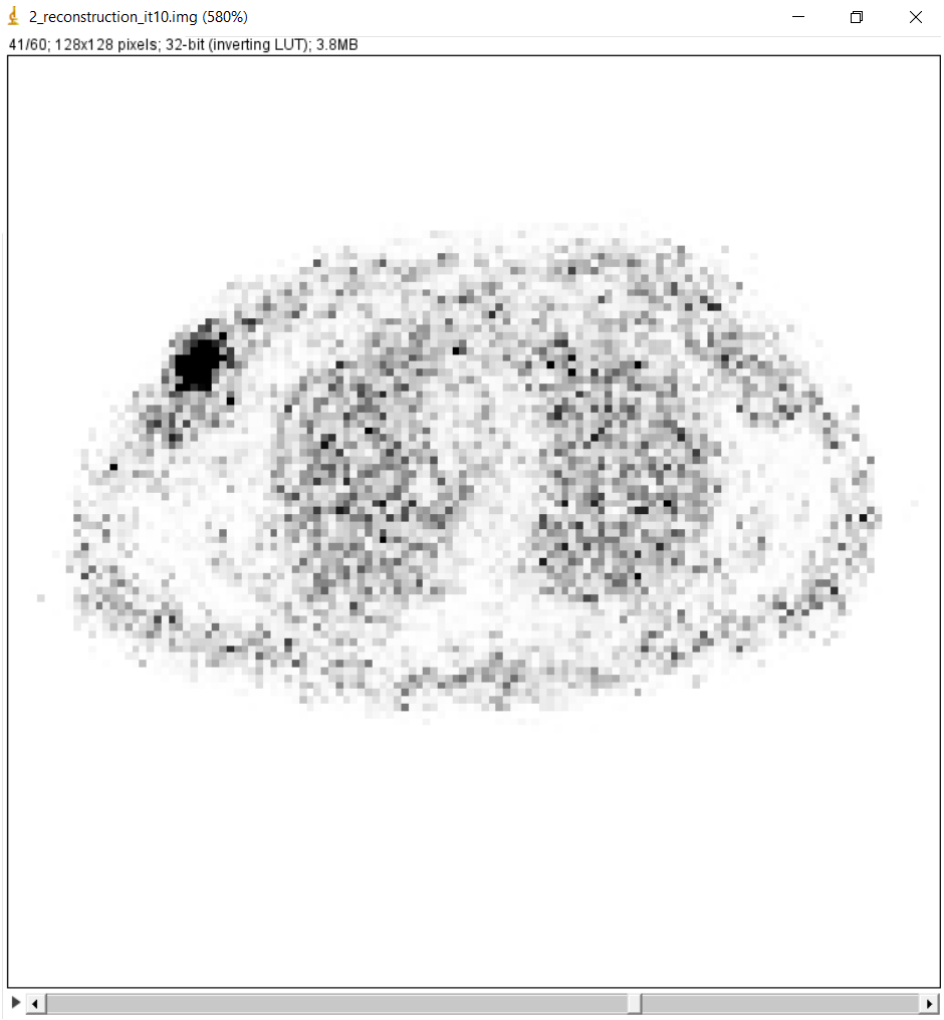

Figure 3.5 View of 41. slice of reconstructed image 2.

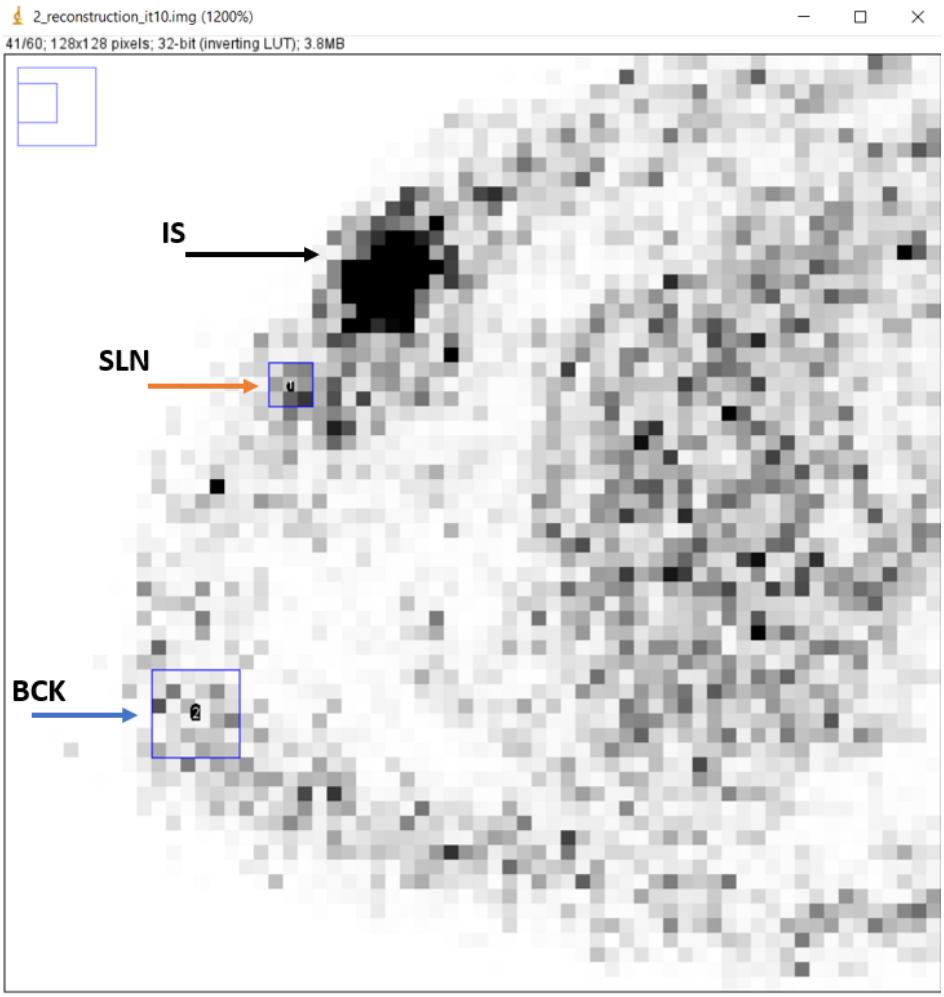

Figure 3.6 Representing to IS, SLN and BCK.

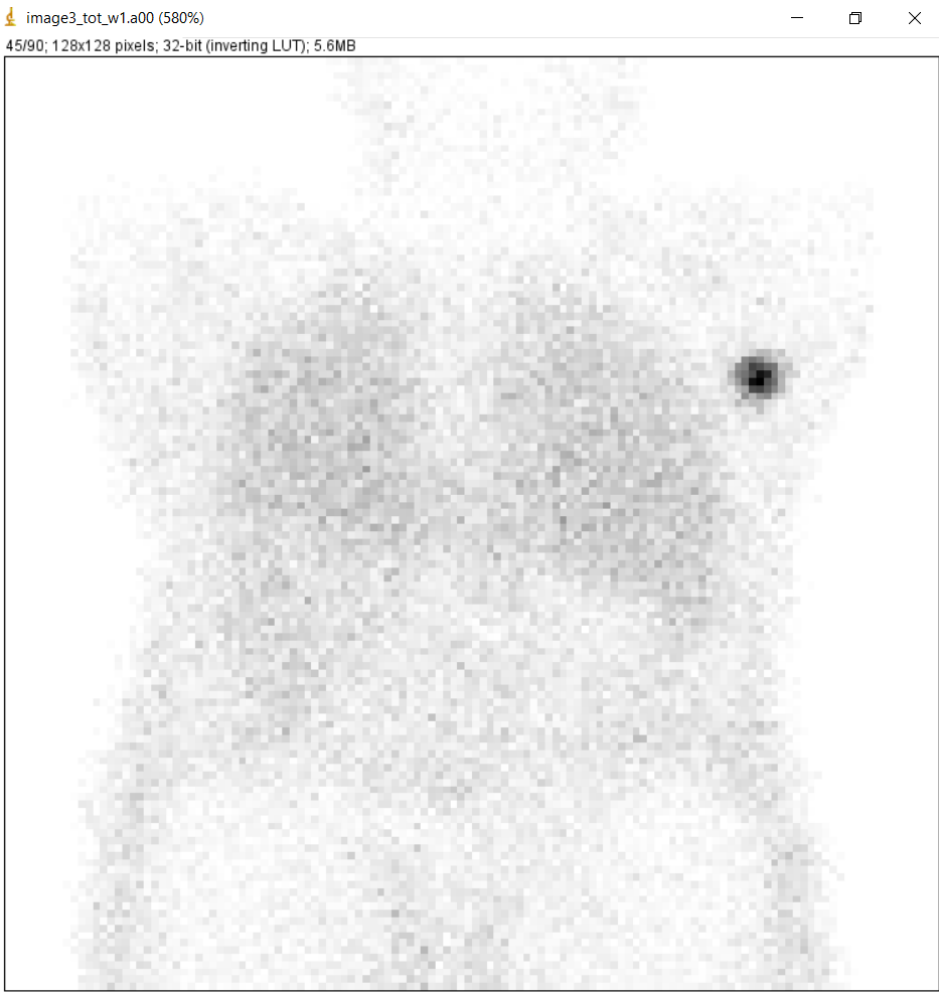

Figure 3.7 View of 45. projection of image 3 with noise.

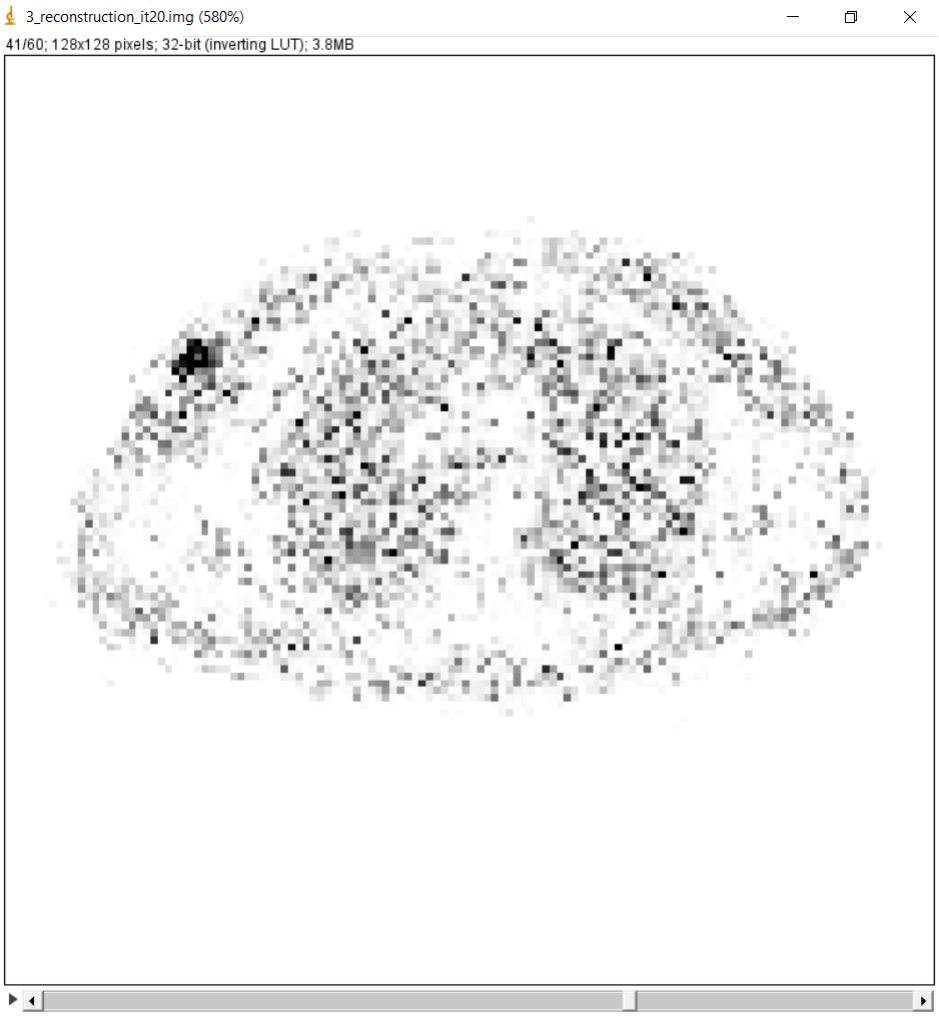

Figure 3.8 View of 41. slice of reconstructed image 3.

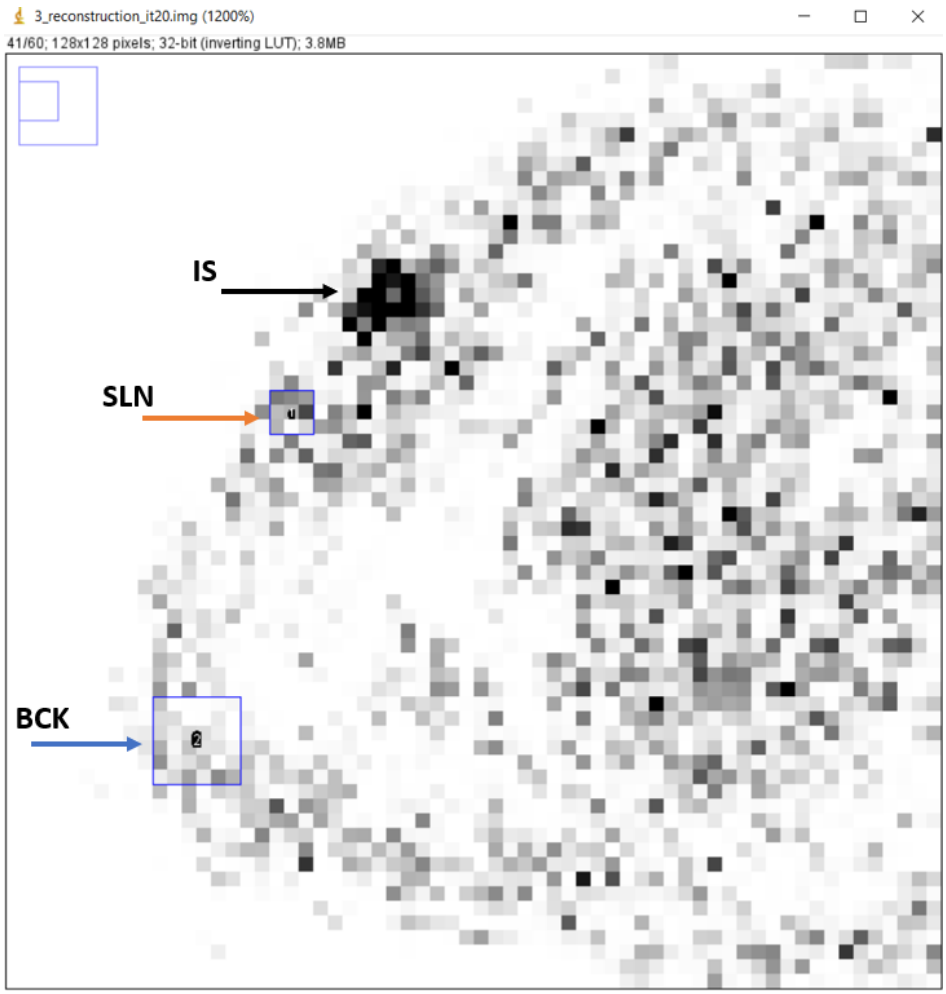

Figure 3.9 Representing to IS, SLN and BCK.

3.2.4 Result for experiment 4

Experiment 4 included LEGP collimator type, 90 projections, and higher count activity level. Upper energy window and lower energy window were set respectively 150.5; 129.5. When the SPECT/CT simulation was run, the noise was not added automatically. Poisson noise was added by Image J program after the acquisition of image (Figure 3.10).

After Poisson noise was added, OSEM reconstruction algorithm was applied with 10 iteration number and 15 subsets. Attenuation correction was included in image 4 (Figure 3.11) and (Figure 3.12).

CNR was used to evaluate the detectability of SLN.

CNR for reconstructed nuclear image 4: **2.76**.

3.2.5 Result for experiment 5

Experiment 5 contained LEHR collimator type, 120 projections, and lower count activity level. Upper energy window and lower energy window were set respectively 150.5; 129.5. When the SPECT/CT simulation was run, the noise was not added automatically. Poisson noise was added by Image J program after the acquisition of image (Figure 3.13).

After Poisson noise was added, OSEM reconstruction algorithm was applied with 10 iteration number and 15 subsets. Attenuation correction was not included in image 5 (Figure 3.14) and (Figure 3.15).

CNR was used to evaluate the detectability of SLN.

CNR for reconstructed nuclear image 5: **5.34**.

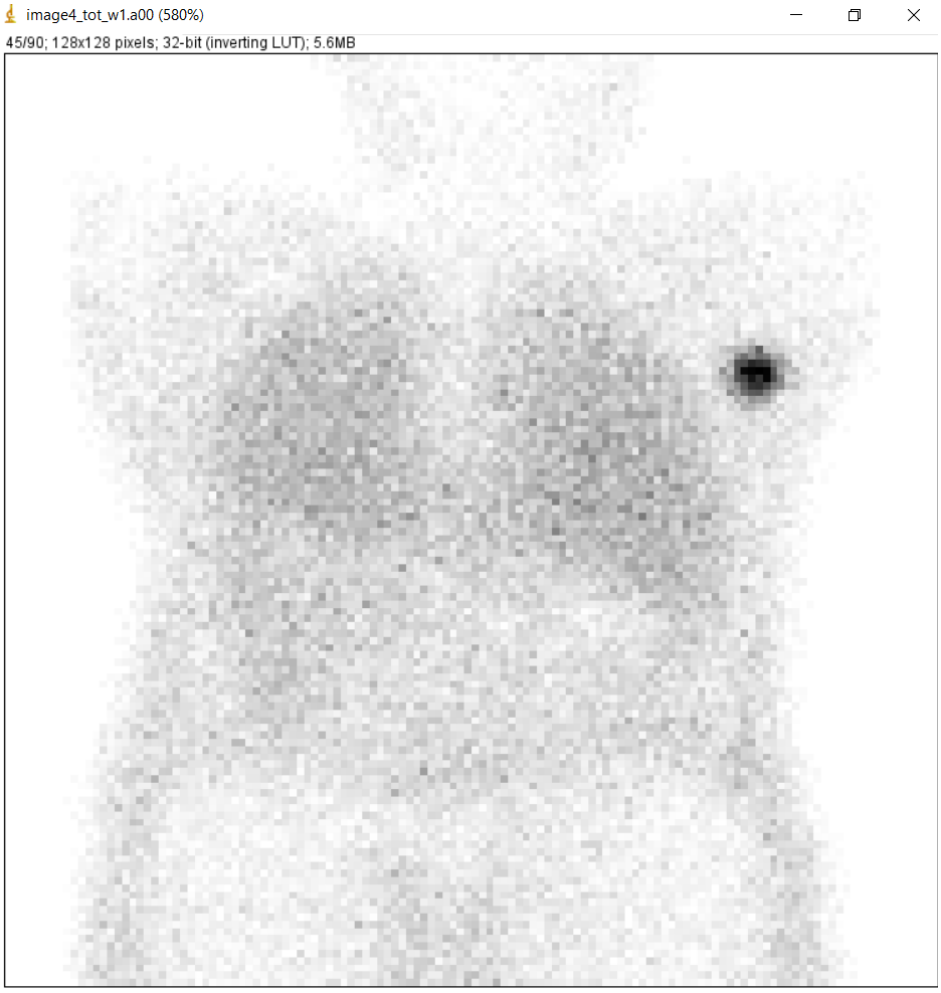

Figure 3.10 View of 45. projection of image 4 with noise.

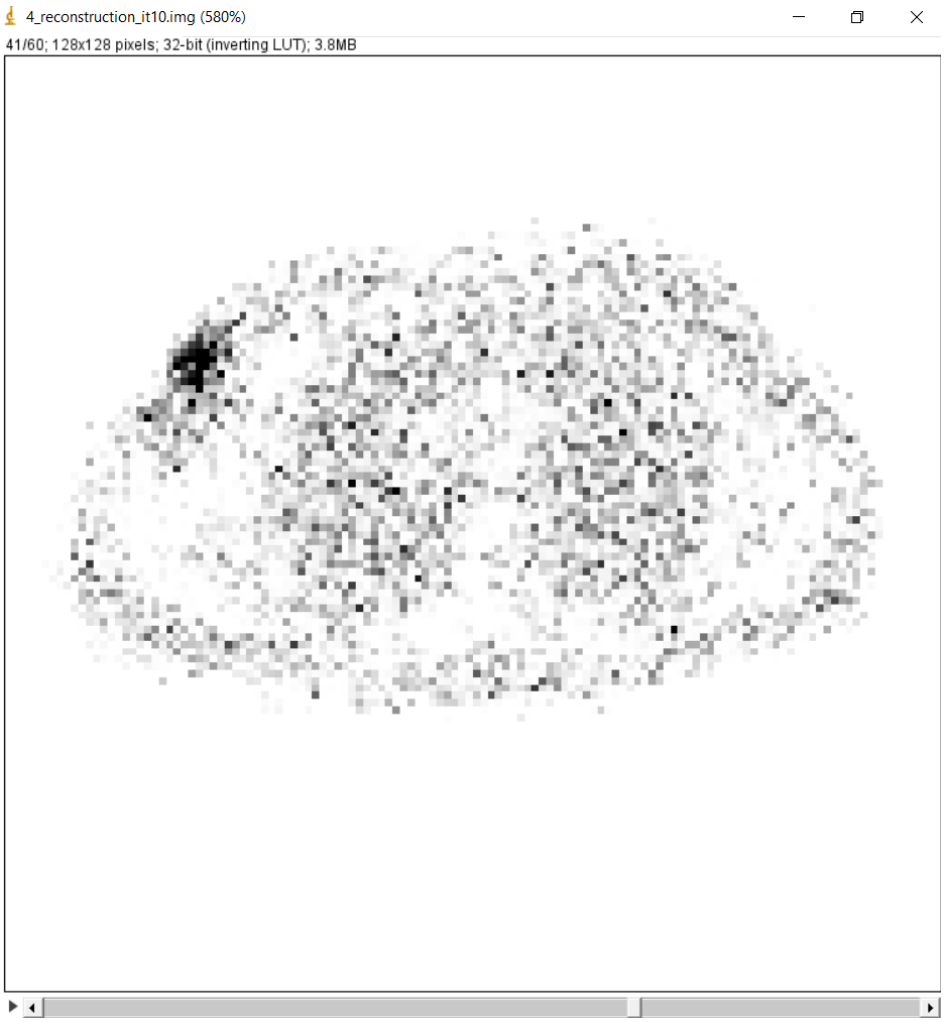

Figure 3.11 View of 41. slice of reconstructed image 4.

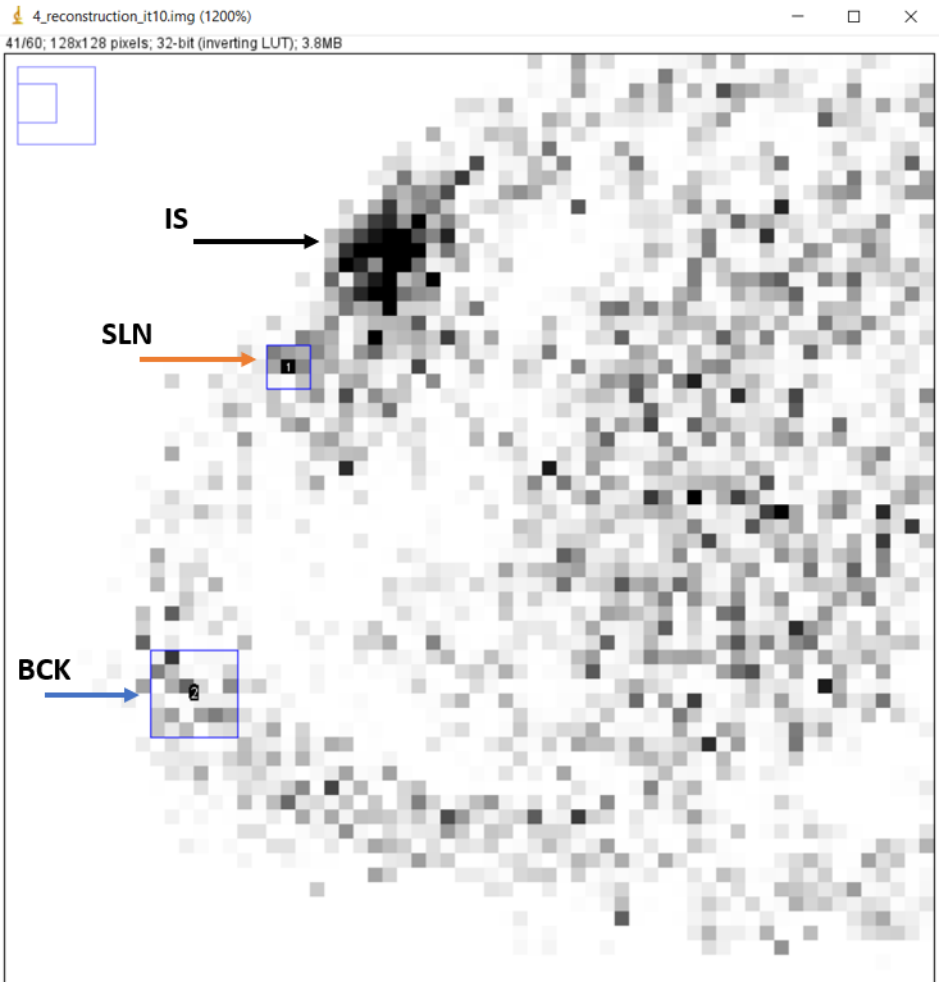

Figure 3.12 Representing to IS, SLN and BCK.

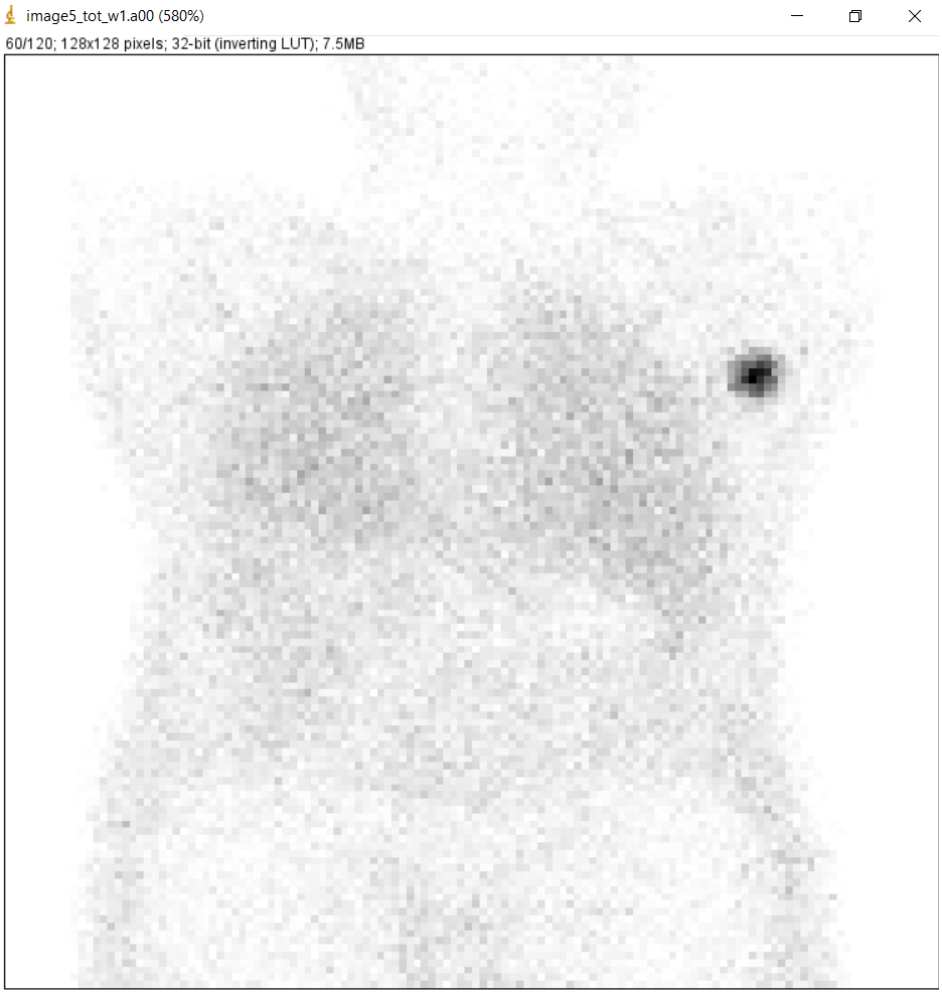

Figure 3.13 View of 60. projection of image 5 with noise.

Figure 3.14 View of 41. slice of reconstructed image 5.

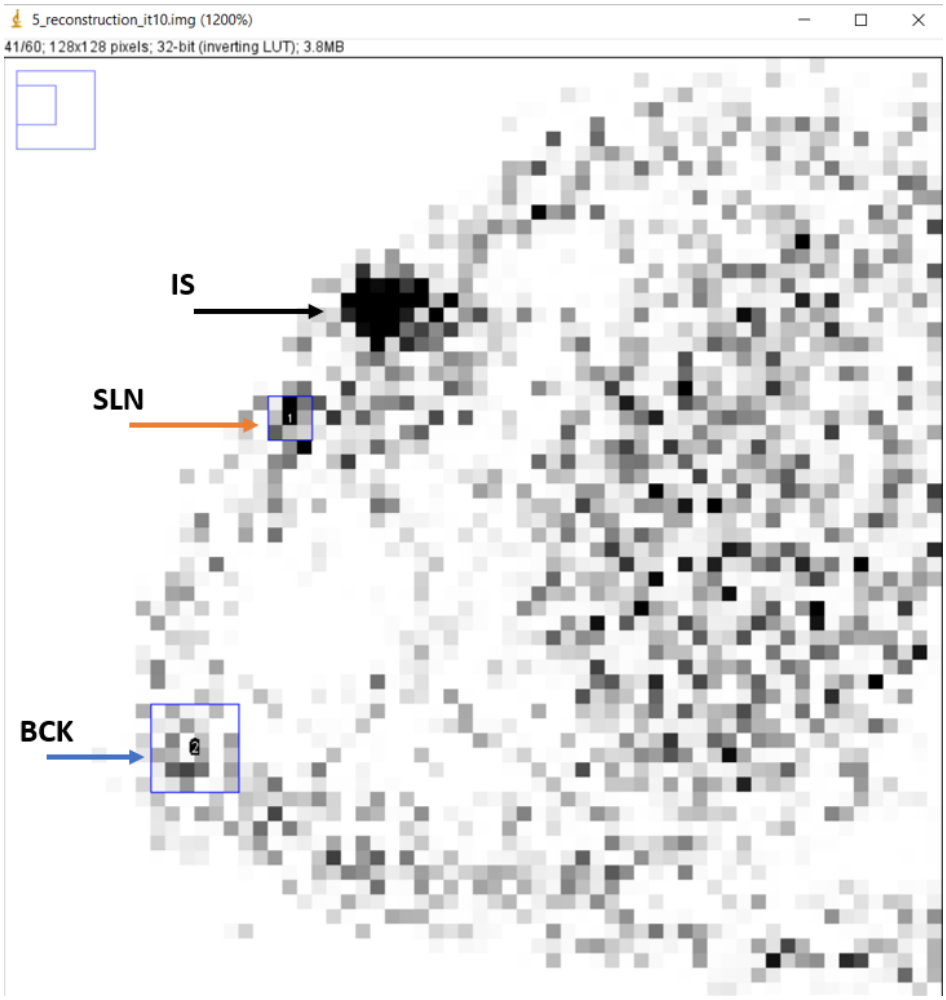

Figure 3.15 Representing to IS, SLN and BCK.

3.2.6 Result for experiment 6

Experiment 6 included LEGP collimator type, 120 projections, and higher count activity level. Upper energy window and lower energy window were set respectively 150.5; 129.5. When the SPECT/CT simulation was run, the noise was not added automatically. Poisson noise was added by Image J program after the acquisition of image (Figure 3.16).

After Poisson noise was added, OSEM reconstruction algorithm was applied with 20 iteration number and 5 subsets. Attenuation correction was not included in image 6 (Figure 3.17) and (Figure 3.18).

CNR was used to evaluate the detectability of SLN.

CNR for reconstructed nuclear image 6: **4.02**.

3.2.7 Result for experiment 7

Experiment 7 comprised LEHR collimator type, 90 projections, and higher count activity level. Upper energy window and lower energy window were set respectively 154; 126. When the SPECT/CT simulation was run, the noise was not added automatically. Poisson noise was added by Image J program after the acquisition of image. Figure 3.19.

After Poisson noise was added, OSEM reconstruction algorithm was applied with 10 iteration number and 5 subsets. Attenuation correction was not included in image 7 (Figure 3.20) and (Figure 3.21).

CNR was used to evaluate the detectability of SLN.

CNR for reconstructed nuclear image 7: **3.9**.

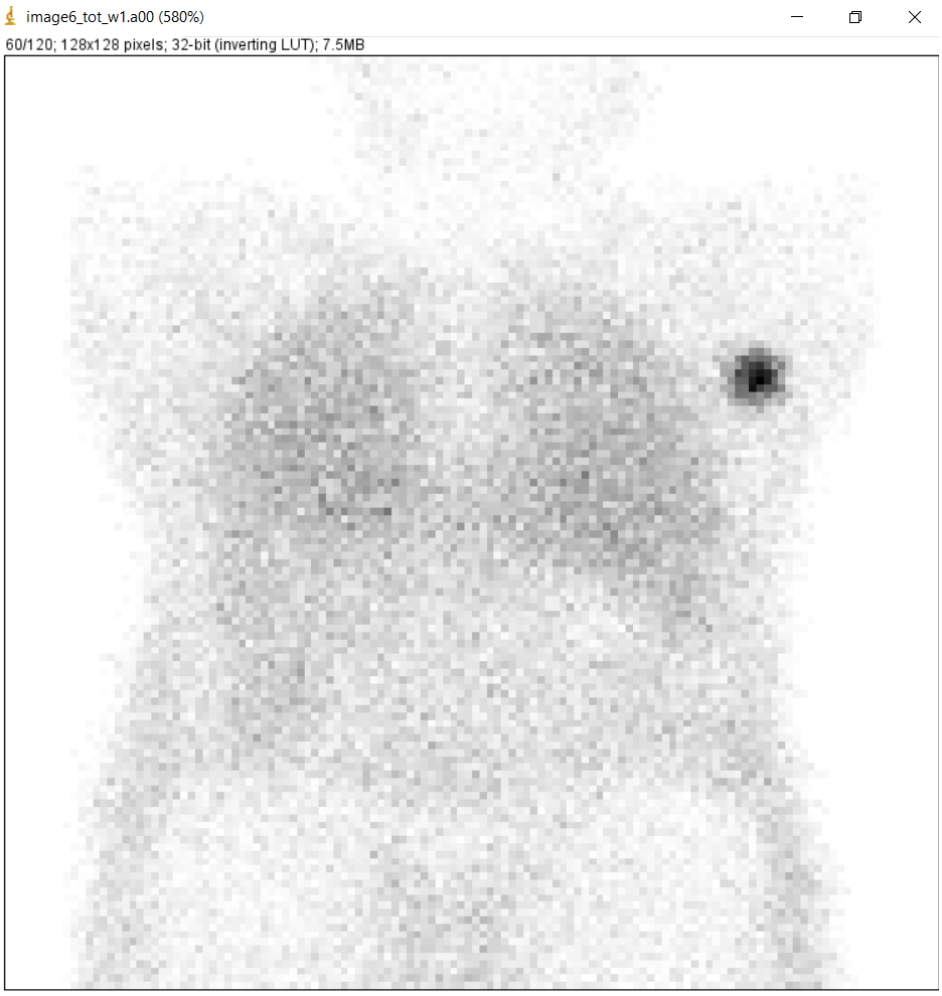

Figure 3.16 View of 60. projection of image 6 with noise.

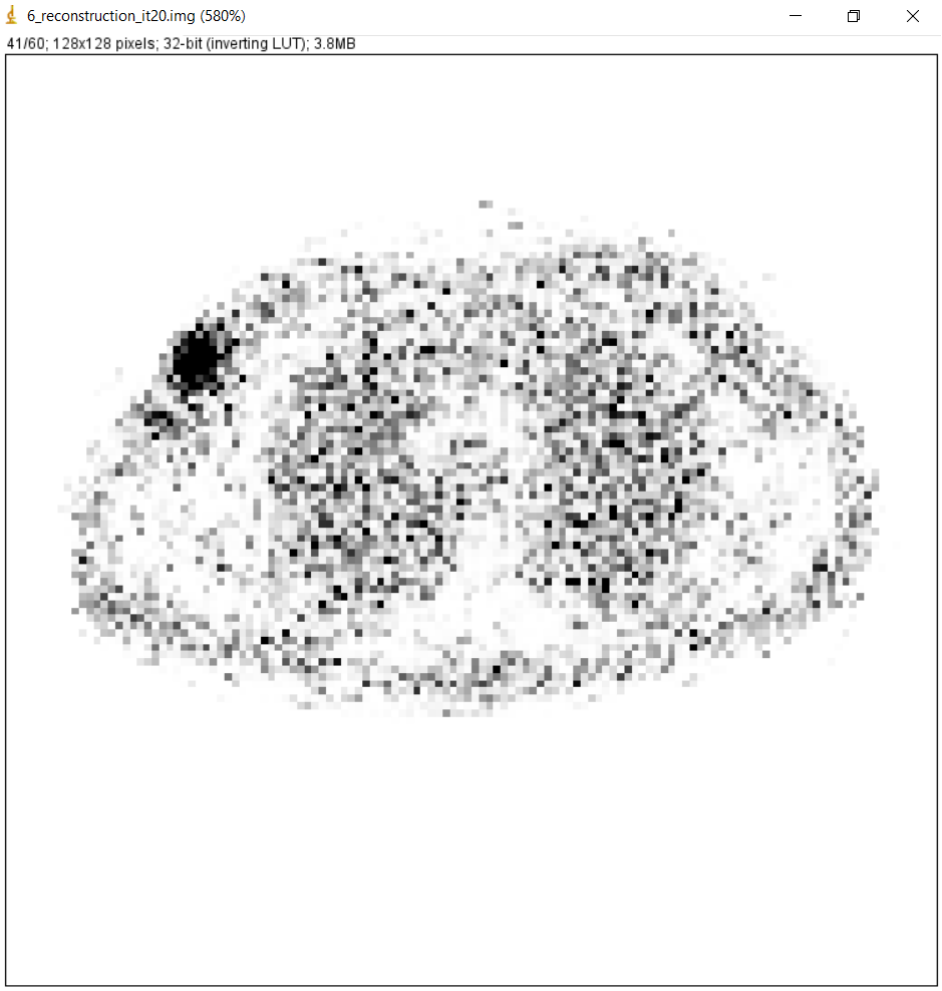

Figure 3.17 View of 41. slice of reconstructed image 6.

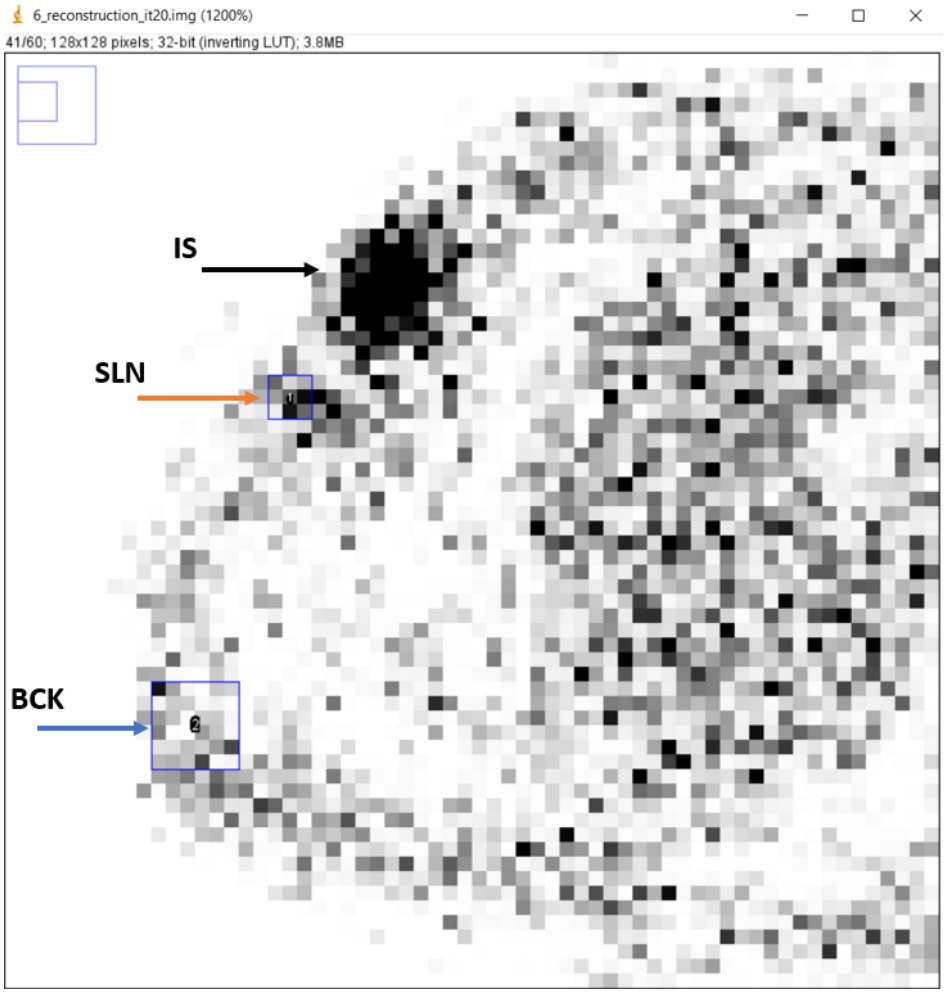

Figure 3.18 Representing to IS, SLN and BCK.

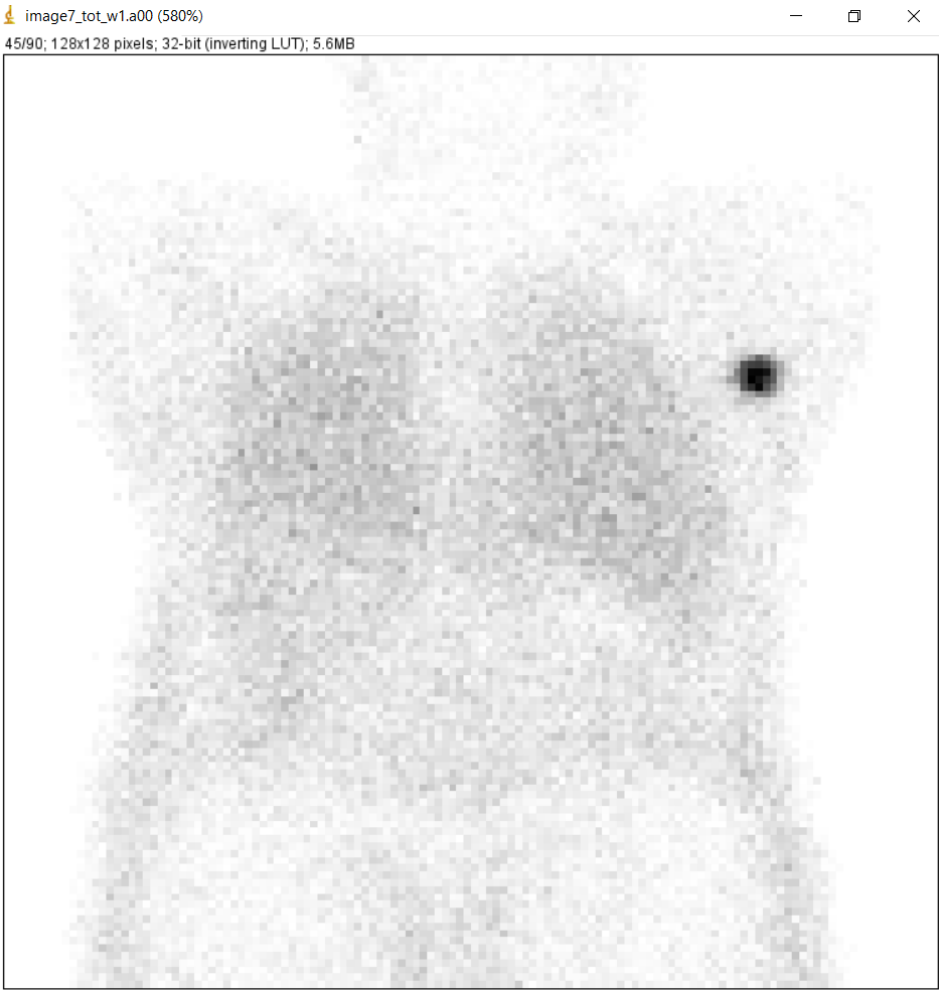

Figure 3.19 View of 45. projection of image 7 with noise.

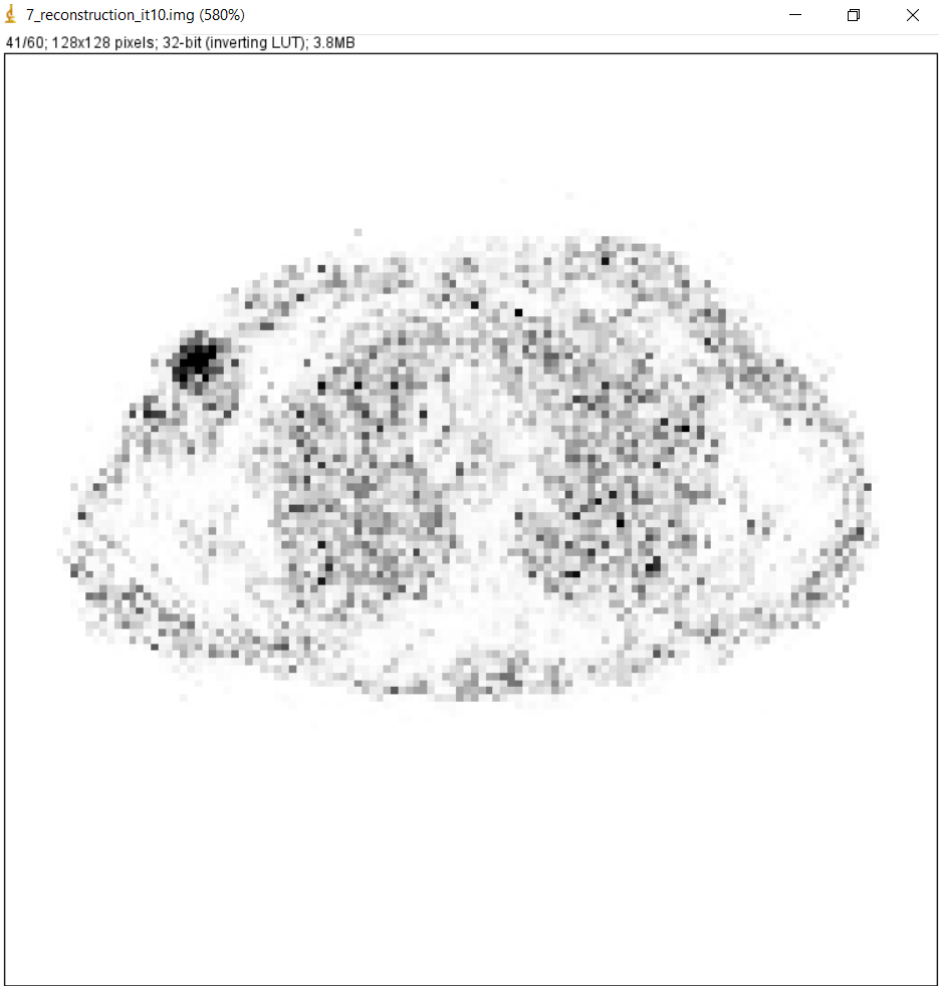

Figure 3.20 View of 41. slice of reconstructed image 7.

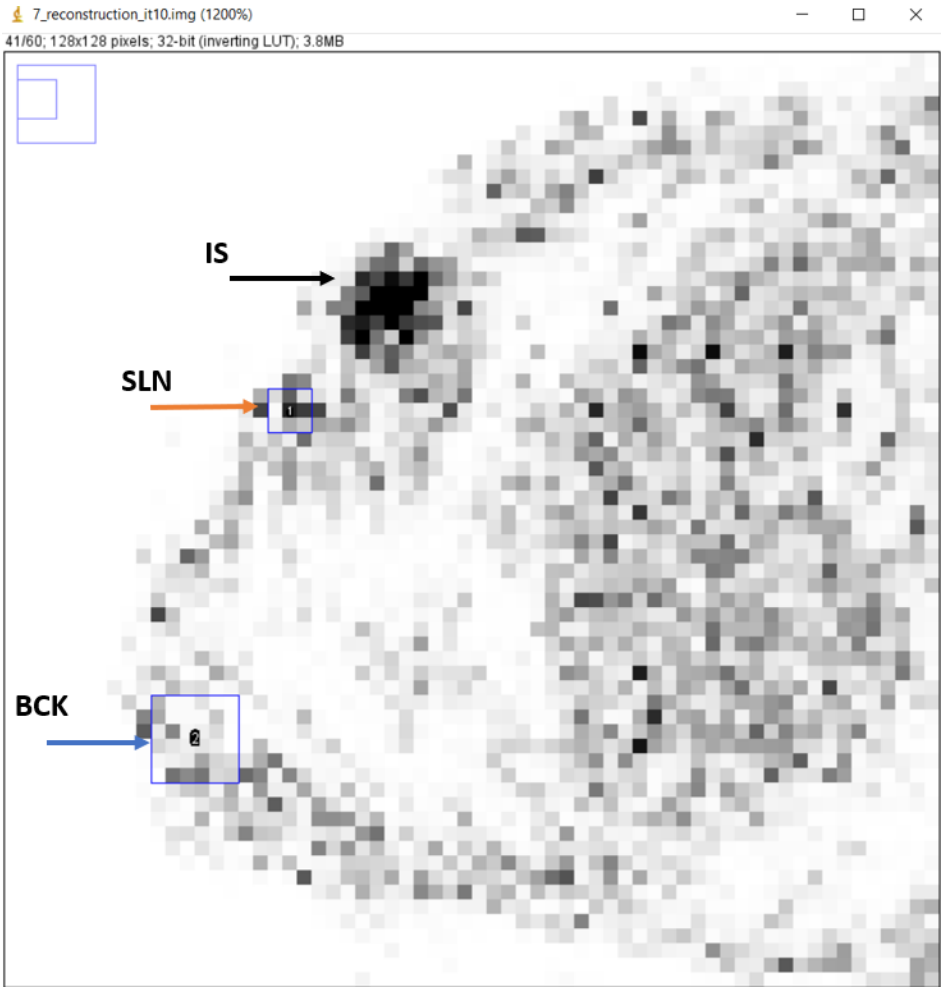

Figure 3.21 Representing to IS, SLN and BCK.

3.2.8 Result for experiment 8

Experiment 8 comprised LEGP collimator type, 90 projections, and lower count activity level. Upper energy window and lower energy window were set respectively 154; 126. When the SPECT/CT simulation was run, the noise was not added automatically. Poisson noise was added by Image J program after the acquisition of image (Figure 3.22).

After Poisson noise was added, OSEM reconstruction algorithm was applied with 20 iteration number and 15 subsets. Attenuation correction was not included in image 8 (Figure 3.23) and (Figure 3.24).

CNR was used to evaluate the detectability of SLN.

CNR for reconstructed nuclear image 8: **2.19**.

3.2.9 Comparison of all images

All images that have been obtained as results of the experiments were demonstrated as comparison figures in Figure 3.25.

Mean values and SD values of SLN and Background in order to calculate Contrast to noise ratios for all experiment showed in table 3.1

3.2.10 The best image and the worst image

The higher contrast to noise ratio was obtained by the combination of LEHR collimator type, higher count activity level, 20 percent energy window, 120 projections, included attenuation correction, 20 iteration number and 15 subsets (Experiment 1).

The lowest contrast to noise ratio was obtained by the combination of LEGP collimator type, lower count activity level, 20 percent energy window, 120 projection number, not-included attenuation correction, 20 iteration number and 15 subsets (Experiment 8).

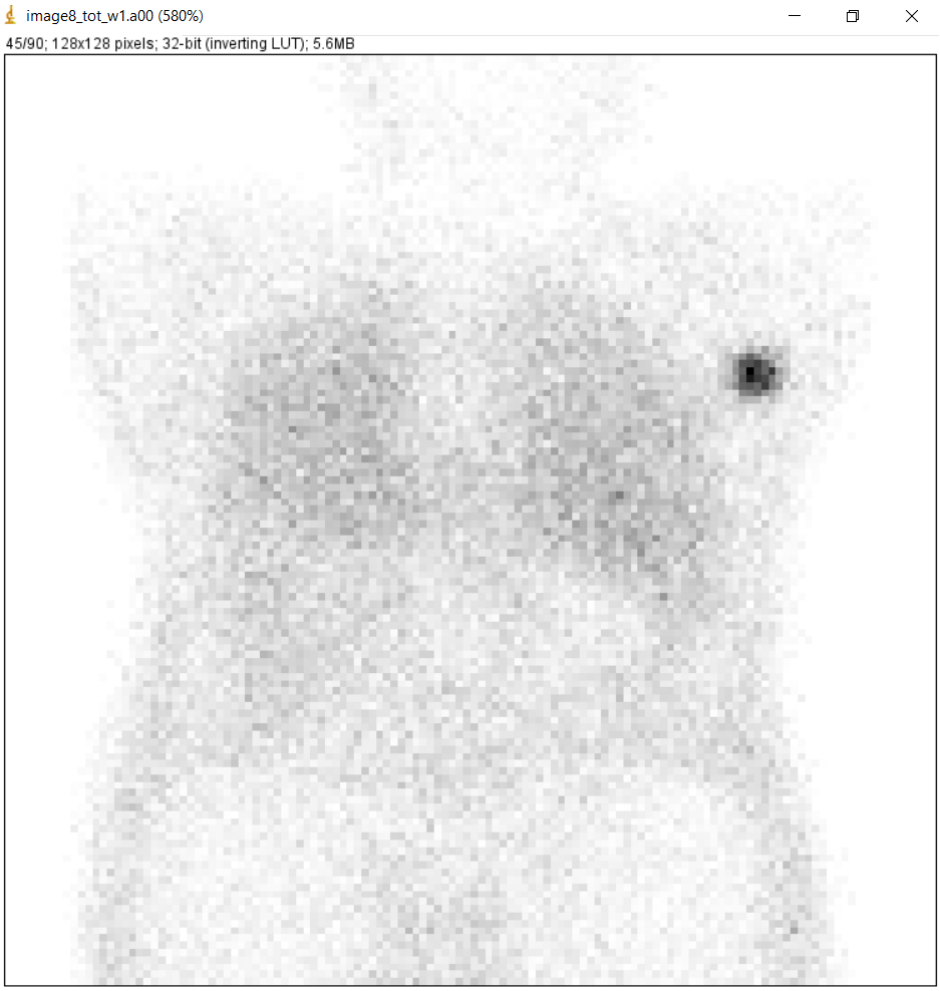

Figure 3.22 View of 45. projection of image 8 with noise.

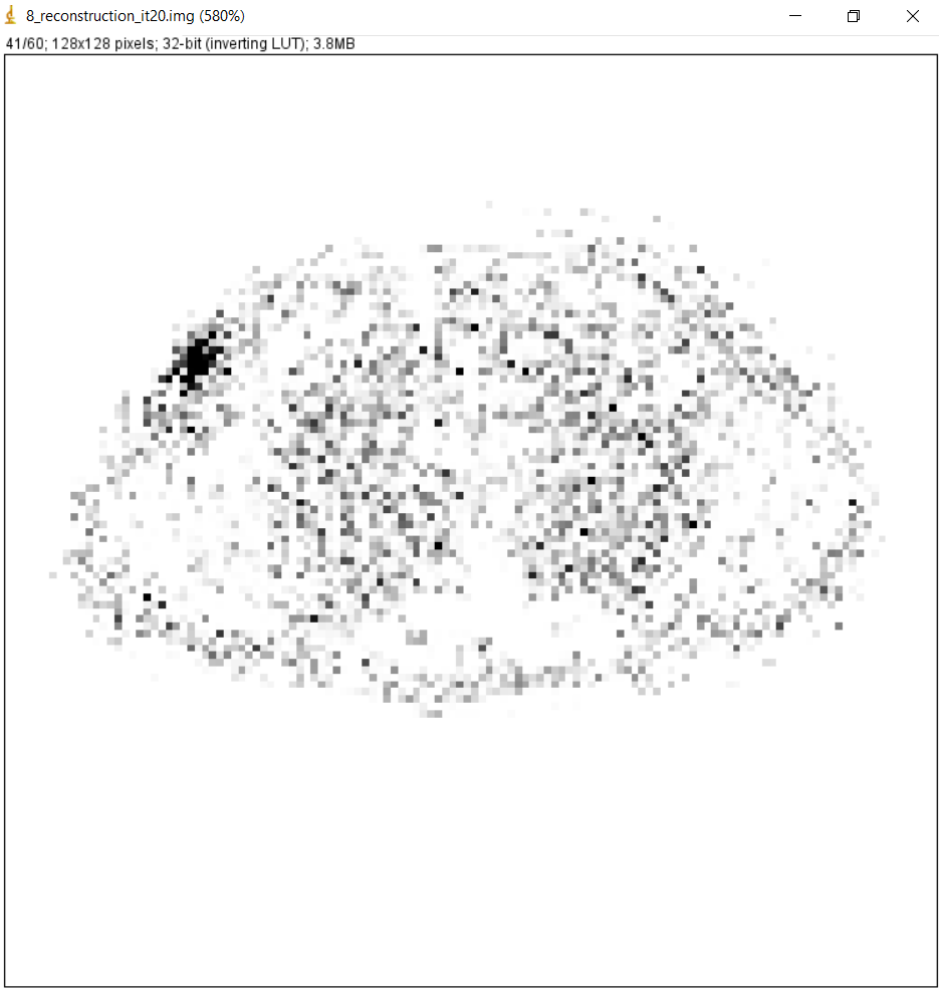

Figure 3.23 View of 41. slice of reconstructed image 8.

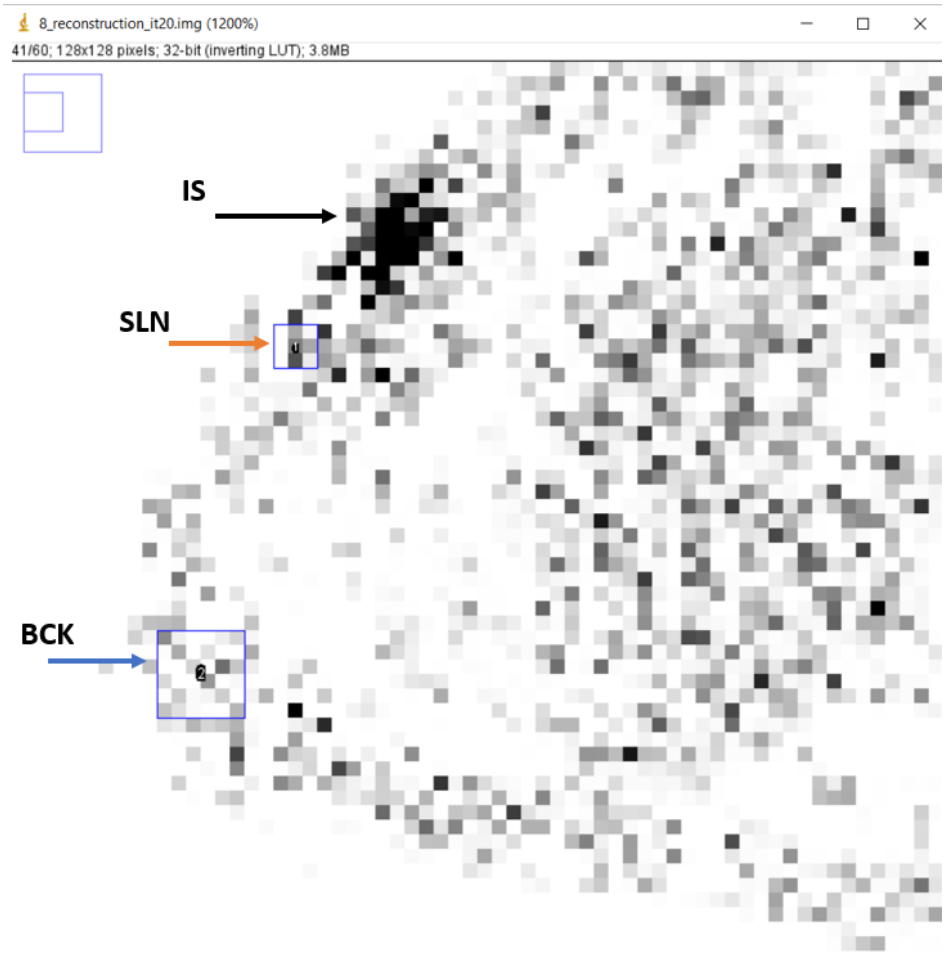

Figure 3.24 Representing to IS, SLN and BCK.

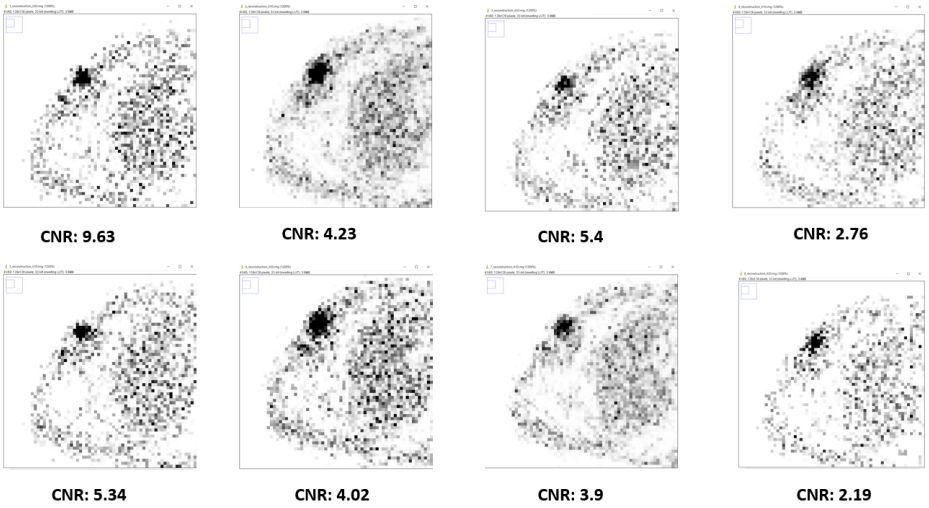

Figure 3.25 Comparison of outputs of experiments.

Table 3.1
Mean values and SD values of SLN and Background.

Label	Area	Mean	SD
Image 1 - SLN	9	275.85	168.98
Image 1 - BCK	36	58.13	68.31
Image 2 - SLN	9	70.40	34.85
Image 2 - BCK	36	31.68	27.41
Image 3 - SLN	9	41.89	25.58
Image 3 - BCK	36	15.01	15.16
Image 4 - SLN	9	338.68	267.26
Image 4 - BCK	36	166.20	187.53
Image 5 - SLN	9	61.90	54.13
Image 5 - BCK	36	21.46	23.11
Image 6 - SLN	9	280.97	170.31
Image 6 - BCK	36	118.87	121.04
Image 7 - SLN	9	167.98	154.32
Image 7 - BCK	36	67.84	76.96
Image 8 - SLN	9	59.67	70.04
Image 8 - BCK	36	29.60	40.59

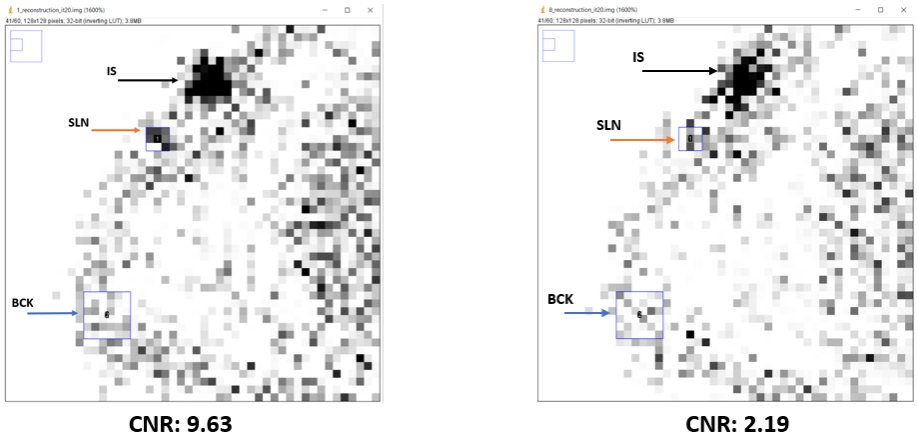

Figure 3.26 The best image and the worst image.

3.2.11 Response Table for Means

Response table for means was acquired as the output of Taguchi Design. This table included parameters names, levels and exhibited their rank in Table 3.2.

Table 3.2
Response Table.

Level	AC	Projection No.	EW	CoT	IT	SU	Count Activity
1	5,505	5,805	4,988	6,067	5,310	4,980	5,077
2	3,862	3,563	4,380	3,300	4,058	4,388	4,290
Delta	1,643	2,243	0,608	2,768	1,253	0,593	0,787
Rank	3	2	6	1	4	7	5

3.2.12 Main Effects Plot for Means

Effect ratios of parameters were represented in Figure 3.27.

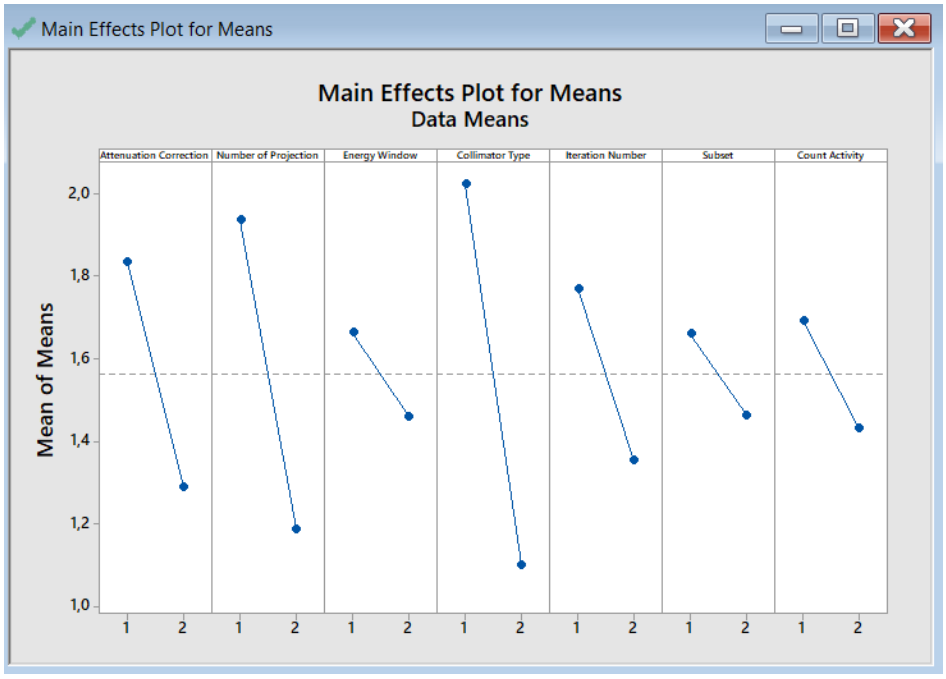

Figure 3.27 Main Effects Plot for Means.

4. DISCUSSION

This study demonstrates that collimator type, projection number, and attenuation correction have remarkably influence on detectability rate of SLNs in the breast.

Attenuation correction is an effective method to increase the accuracy of images. Many studies have put forward that attenuation correction improves the image quality unlike scatter correction that makes SLNs invisible [3]. This study supports the present articles.

Evaluation of collimator types also has a considerable place in the literature in order to increase the visibility of SLNs [11]. LEHR collimator type is one of the preferred collimator types to represent SLNs. A study shows that LMEGP collimator enhances image quality compared to LEHR and MELP[11]. LMEGP is not available in SIMIND Monte Carlo Simulation, so LEHR and LEGP are evaluated in this study. Characteristics of LEGP have not examined in literature for SLNs in the breast. Therefore, comparison of the ratio of the difference between LEHR and LEGP according to literature cannot succeed. Yet, distinct collimator types are expected to have different and significant effects on the image.

Small sampling number of projection data are preferred owing to shorter acquisition time. However, increasing the projection number enhances image quality [20],[21]. So, higher projection number can be used for small size SLNs since difficult to represent small size SLNs especially when they are close the injection site [22],[23].

Previous studies show that the iteration number is an important parameter for image quality. When iteration number boosts, the detectability and visibility of the lesion develop [24]. This study supports the findings.

According to a study published in 2013, the optimal subset number cannot be identified [12]. This study demonstrates that there is no considerable impact of subset number on image quality.

When count activity doubled, the noise decreases about 1.4 times. It leads to more

the detectability ratio of SLNs.

Some restrictions were encountered during this study. First of them is that breast cancer is experienced by women. Yet, Zubal torso is a man torso. Secondly, scatter correction make the SLN invisible because of its small size. Scatter correction is needed to check in greater size SLNs.

5. CONCLUSIONS

One of the purposes of the study was to find out which parameters have more influence on image quality in SPECT/CT imaging. Collimator type, projection number, and attenuation correction were found to have the highest effect on SLN detectability compared to other parameters. However, all parameters except subset have substantial effects on image quality.

Another aim was to examine which levels are more beneficial for the detectability of SLNs in the breast. According to response table, attenuation correction compared favorably with respect to no attenuation correction; 120 projections compared favorably with respect to 90 projections, LEHR collimator type compared favorably with respect to LEGP collimator type; 20% energy window compared favorably with respect to 15% energy window, 20 iterations compared favorably with respect to 10 iterations and higher count activity level compared favorably with respect to lower count activity level.

REFERENCES

1. Madsen, M., "Recent advances in spect imaging. journal of nuclear medicine," ,, Vol. 48, no. 4, pp. 661–673, 2007.

2. Holmberg, D., "Optimisation of image acquisition and reconstruction of 111in-pentetrotide spect," 2012.

3. Buck, A. K., S. Nekolla, S. Ziegler, A. Beer, B. J. Krause, K. Herrmann, K. Scheidhauer, H.-J. Wester, E. J. Rummeny, M. Schwaiger, *et al.*, "Spect/ct," *Journal of Nuclear Medicine*, Vol. 49, no. 8, pp. 1305–1319, 2008.

4. Pouw, B., D. Hellingman, M. Kieft, W. V. Vogel, K. J. van Os, E. Rutgers, R. V. Olmos, and M. P. Stokkel, "The hidden sentinel node in breast cancer: Reevaluating the role of spect/ct and tracer reinjection," *European Journal of Surgical Oncology (EJSO)*, Vol. 42, no. 4, pp. 497–503, 2016.

5. Simanek, M., and P. Koranda, "Spect/ct imaging in breast cancer-current status and challenges.," *Biomedical Papers of the Medical Faculty of Palacky University in Olomouc*, Vol. 160, no. 4, 2016.

6. Mathelin, C., S. Salvador, D. Huss, and J.-L. Guyonnet, "Precise localization of sentinel lymph nodes and estimation of their depth using a prototype intraoperative mini γ-camera in patients with breast cancer," *Journal of Nuclear Medicine*, Vol. 48, no. 4, pp. 623–629, 2007.

7. Uren, R., R. Howman-Giles, D. Chung, A. Spillane, F. Noushi, D. Gillett, L. Gluch, C. Mak, R. West, J. Briody, *et al.*, "Spect/ct scans allow precise anatomical location of sentinel lymph nodes in breast cancer and redefine lymphatic drainage from the breast to the axilla," *The Breast*, Vol. 21, no. 4, pp. 480–486, 2012.

8. Cserni, G., "Mapping metastases in sentinel lymph nodes of breast cancer," *American journal of clinical pathology*, Vol. 113, no. 3, pp. 351–354, 2000.

9. Martin, R. C., J. Fey, H. Yeung, P. I. Borgen, and H. S. Cody, "Highest isotope count does not predict sentinel node positivity in all breast cancer patients," *Annals of surgical oncology*, Vol. 8, no. 7, pp. 592–597, 2001.

10. Yoneyama, H., H. Tsushima, M. Onoguchi, T. Konishi, K. Nakajima, S. Matsuo, D. Kayano, H. Wakabayashi, A. Inaki, and S. Kinuya, "Optimization of attenuation and scatter corrections in sentinel lymph node scintigraphy using spect/ct systems," *Annals of nuclear medicine*, Vol. 29, no. 3, pp. 248–255, 2015.

11. Yoneyama, H., H. Tsushima, M. Kobayashi, M. Onoguchi, K. Nakajima, and S. Kinuya, "Improved detection of sentinel lymph nodes in spect/ct images acquired using a low- to medium-energy general-purpose collimator," *Clinical nuclear medicine*, Vol. 39, no. 1, pp. e1–e6, 2014.

12. Okuda, K., K. Nakajima, M. Yamada, H. Wakabayashi, H. Ichikawa, H. Arai, S. Matsuo, J. Taki, M. Hashimoto, and S. Kinuya, "Optimization of iterative reconstruction parameters with attenuation correction, scatter correction and resolution recovery in myocardial perfusion spect/ct," *Annals of nuclear medicine*, Vol. 28, no. 1, pp. 60–68, 2014.

13. Loudos, G. K., "Monte carlo simulations in nuclear medicine," in *AIP Conference Proceedings*, Vol. 958, pp. 147–150, AIP, 2007.

14. Ljungberg, M., S. Strand, and M. King, "The simind monte carlo program," *Monte Carlo calculation in nuclear medicine: Applications in diagnostic imaging. Bristol: IOP Publishing*, pp. 145–63, 1998.

15. Schepis, T., O. Gaemperli, P. Koepfli, C. Rüegg, C. Burger, S. Leschka, L. Desbiolles, L. Husmann, H. Alkadhi, and P. A. Kaufmann, "Use of coronary calcium score scans from stand-alone multislice computed tomography for attenuation correction of myocardial perfusion spect," *European journal of nuclear medicine and molecular imaging*, Vol. 34, no. 1, pp. 11–19, 2007.

16. Alqahtani, M., J. Lees, S. Bugby, L. Jambi, and A. Perkins, "Lymphoscintigraphic imaging study for quantitative evaluation of a small field of view (sfov) gamma camera," *Journal of Instrumentation*, Vol. 10, no. 07, p. P07011, 2015.

17. Roy, R. K., *Design of experiments using the Taguchi approach: 16 steps to product and process improvement*, John Wiley & Sons, 2001.

18. Morris, M., *Design of experiments: an introduction based on linear models*, Chapman and Hall/CRC, 2010.

19. Sabondjian, E., A. J. Mitchell, G. Wisenberg, J. White, K. J. Blackwood, J. Sykes, L. Deans, R. Z. Stodilka, and F. S. Prato, "Hybrid spect/cardiac-gated first-pass perfusion ct: locating transplanted cells relative to infarcted myocardial targets," *Contrast media & molecular imaging*, Vol. 7, no. 1, pp. 76–84, 2012.

20. Chan, H.-P., M. M. Goodsitt, M. A. Helvie, S. Zelakiewicz, A. Schmitz, M. Noroozian, C. Paramagul, M. A. Roubidoux, A. V. Nees, C. H. Neal, *et al.*, "Digital breast tomosynthesis: observer performance of clustered microcalcification detection on breast phantom images acquired with an experimental system using variable scan angles, angular increments, and number of projection views," *Radiology*, Vol. 273, no. 3, pp. 675–685, 2014.

21. Takahashi, Y., K. Murase, T. Mochizuki, H. Higashino, Y. Sugawara, and A. Kinda, "Evaluation of the number of spect projections in the ordered subsets-expectation maximization image reconstruction method," *Annals of nuclear medicine*, Vol. 17, no. 7, pp. 525–530, 2003.

22. Vercellino, L., J. Ohnona, D. Groheux, A. Slama, P. M. Colletti, S. Chondrogiannis, P. Merlet, M.-E. Toubert, and D. Rubello, "Role of spect/ct in sentinel lymph node detection in patients with breast cancer," *Clinical nuclear medicine*, Vol. 39, no. 5, pp. 431–436, 2014.

23. van der Ploeg, I. M., O. E. Nieweg, B. B. Kroon, E. J. Rutgers, M.-J. T. B.-V. Peeters, W. V. Vogel, C. A. Hoefnagel, and R. A. V. Olmos, "The yield of spect/ct for anatomical lymphatic mapping in patients with breast cancer," *European journal of nuclear medicine and molecular imaging*, Vol. 36, no. 6, pp. 903–909, 2009.

24. Katua, A., A. Ankrah, M. Vorster, A. Van Gelder, and M. Sathekge, "Optimization of ordered subset expectation maximization reconstruction for reducing urinary bladder artifacts in single-photon emission computed tomography imaging," *World journal of nuclear medicine*, Vol. 10, no. 1, p. 3, 2011.